

# CellEcoNet: Decoding the Cellular Language of Pathology with Deep Learning for Invasive Lung Adenocarcinoma Recurrence Prediction

Abdul Rehman Akbar<sup>1,6</sup>, Usama Sajjad<sup>1</sup>, Ziyu Su<sup>1</sup>, Wencheng Li<sup>2</sup>, Fei Xing<sup>3</sup>, Jimmy Ruiz<sup>4,5</sup>, Wei Chen<sup>1</sup>, Muhammad Khalid Khan Niazi<sup>1</sup>

<sup>1</sup> Department of Pathology, College of Medicine, The Ohio State University Wexner Medical Center, Columbus, OH, USA

<sup>2</sup> Department of Pathology, Wake Forest University School of Medicine, Winston-Salem, NC, USA

<sup>3</sup> Department of Cancer Biology, Wake Forest University School of Medicine, Winston-Salem, NC, USA

<sup>4</sup> Department of Medicine (Hematology & Oncology), Wake Forest University School of Medicine, Winston-Salem, NC, USA

<sup>5</sup> Section of Hematology & Oncology, W.G. (Bill) Hefner Veterans Affairs Medical Center (VAMC), Salisbury, NC, USA

<sup>6</sup> Lead Contact

## Abstract

Despite surgical resection, ~70% of invasive lung adenocarcinoma (ILA) patients recur within five years, and current tools fail to identify those needing adjuvant therapy. To address this unmet clinical need, we introduce **CellEcoNet**, a novel spatially aware deep learning framework that models whole slide images (WSIs) through natural language analogy, defining a “language of pathology,” where cells act as words, cellular neighborhoods become phrases, and tissue architecture forms sentences. CellEcoNet learns these context-dependent meanings automatically, capturing how subtle variations and spatial interactions derive recurrence risk. On a dataset of **456** H&E-stained WSIs, CellEcoNet achieved superior predictive performance (**AUC:77.8% HR:9.54**), outperforming IASLC grading system (AUC:71.4% HR:2.36), AJCC Stage (AUC:64.0% HR:1.17) and state-of-the-art computational methods (AUCs:62.2-67.4%). CellEcoNet demonstrated fairness and consistent performance across diverse demographic and clinical subgroups. Beyond prognosis, CellEcoNet marks a paradigm shift by decoding the tumor microenvironment’s cellular “language” to reveal how subtle cell variations encode recurrence risk.

## 1. Introduction

Lung adenocarcinoma, the most common histological subtype of non-small cell lung cancer (NSCLC), remains a leading cause of cancer-related death worldwide, accounting for over 40% of NSCLC cases and contributing to more than 1.7 million deaths annually [1, 2]. Even among patients with early-stage invasive lung adenocarcinoma (ILA) who undergo curative-intent

surgical resection, long-term prognosis remains poor, as approximately 30–40% will experience recurrence within five years [3, 4], and the overall 5-year survival rate for ILA remains near 25% [5]. This persistent risk underscores the critical need for better prognostic tools to guide postoperative care.

Accurate recurrence prediction is essential for personalized treatment strategies. High-risk patients may benefit from adjuvant therapy and closer surveillance, whereas low-risk patients could avoid unnecessary overtreatment and its associated toxicities [6]. However, current prognostic tools offer alarmingly limited predictive value. The tumor node metastasis (TNM) staging system, considered the gold standard for treatment decisions, achieves only modest prognostic performance for overall survival prediction [7-9]. Even more concerning, studies specifically evaluating recurrence prediction show that TNM staging achieves an area under the curve (AUC) of merely  $0.561 \pm 0.042$ , while tumor grading performs only marginally better at  $0.573 \pm 0.044$  [10]. Histologic subtyping, despite recent advances in the International Association for the Study of Lung Cancer (IASLC) grading system, demonstrates AUCs ranging from 0.68-0.70 for recurrence-free survival [11]. These disappointing results stem from inherent limitations including interobserver variability and inability of these coarse-grained systems to capture the complex biological heterogeneity of tumors [12, 13]. There is thus an urgent need for more robust, biologically informed histopathological signals that can capture the complex cellular and architectural features underlying tumor heterogeneity, which when integrated with molecular and clinical data, could enable the development of comprehensive prognostic tools with superior predictive accuracy.

The advent of digital pathology has revolutionized cancer research by enabling computational analysis of whole slide images (WSIs) of hematoxylin and eosin (H&E)-stained tissue sections, which contain rich information about tumor architecture, cellular morphology, and the tumor microenvironment (TME) that may harbor high-dimensional prognostic signals invisible to the naked eye [14, 15]. However, extracting meaningful signals from these gigapixel-sized images remains a significant challenge.

Deep learning (DL) has shown promise in analyzing WSIs for tasks such as tumor classification and grading [16]. Current DL models, often referred to as foundation models, in computational pathology are trained using objectives that fundamentally misalign with clinical needs. These foundation models typically pursue two primary objectives: reconstructing masked regions of images from unmasked portions—an approach that may ask the model to reconstruct stromal tissue from neutrophil patterns, which lacks biological coherence; and making representations of different views of the same image similar, which may capture superficial features like color information while ignoring the rich histological details. While these training paradigms have proven remarkably effective in general computer vision tasks using natural images, their application to histopathology reveals a fundamental mismatch between methodology and domain characteristics.

This divergence becomes particularly evident when contrasting language models versus vision models in specialized domains. Language models have achieved unprecedented success through a crucial architectural insight: natural language possesses inherent hierarchical building blocks, alphabets combine to form words, words assemble into phrases, phrases construct sentences, sentences build paragraphs, and paragraphs create documents. Language models explicitly encode these structural elements through tokenization, positional encoding, and hierarchical attention mechanisms, allowing them to capture meaning at multiple scales simultaneously. Each token (word) is understood through its relationships with neighboring tokens, creating rich contextual embeddings that shift meaning based on linguistic context.

In stark contrast, vision models, particularly in medical imaging, have not achieved comparable success despite substantial computational investment[17]. This disparity arises because most images lack the clear hierarchical building blocks that make language so amenable to computational modeling. Traditional image analysis approaches apply vision architectures derived from natural image processing, where arbitrary patch divisions serve as the fundamental units of analysis.

Remarkably, histopathological images represent a unique exception: they possess intrinsic biological building blocks analogous to linguistic structures. Individual cells serve as fundamental "words" of tissue architecture, cellular neighborhoods function as "phrases," tissue regions act as "sentences," and WSIs constitute complete biological "documents." Just as linguistic meaning is context-dependent—where "apple" denotes a fruit in "she ate an apple" but refers to a technology company in "she bought a new Apple product"—the biological significance of cells is determined by their spatial neighbors, morphological state, and microenvironmental interactions. For instance, epithelial cells acquire distinct biological significance based on context: an elongated epithelial cell within a stromal-rich region may indicate epithelial-mesenchymal transition, whereas a cuboidal epithelial cell organized within a glandular structure represents normal differentiation.

Despite this compelling biological analogy, computational pathology remains largely unexplored from a language modeling perspective. Most existing approaches derive inspiration from computer vision models designed for natural images [18], fundamentally misunderstanding the structured, hierarchical nature of biological tissues. This represents a significant missed opportunity to systematically explore how principles that made language models successful—explicit tokenization, contextual embeddings, hierarchical attention, and structured sequence modeling—might revolutionize tissue biology understanding and disease prediction.

To overcome these fundamental limitations, we introduce CellEcoNet, a spatially aware DL framework that models the TME as a dynamic, multiscale cell ecology. CellEcoNet operates at the cellular level by tokenizing individual nuclei rather than arbitrary image patches. In this formulation, each cell acts like a "word," and spatial configurations of cells form biologically meaningful "sentences." CellEcoNet defines a "language for pathology," where intra-cellular

variations correspond to contextual variability, and inter-cellular spatial relationships convey context, function, and prognosis. By integrating high-resolution cellular features with tissue-level architectural context and explicitly modeling diverse cell types, CellEcoNet constructs a spatially resolved map of cell ecology, capturing emergent properties such as niche formation, cellular cooperation, and immune evasion that govern recurrence risk. In doing so, CellEcoNet not only improves predictive accuracy, but also offers a conceptual shift i.e., WSIs are no longer viewed as static mosaics of patches, but as dynamic biological texts, whose grammar is shaped by cell types, spatial proximity, and microenvironmental interactions. This ecology-inspired framework provides a novel foundation for building interpretable and clinically actionable AI tools in pathology.

## 2 Methods

Multiple instance learning (MIL) has emerged as the dominant framework in computational pathology for handling weak supervision, treating WSIs as bags of instances with only slide-level labels [19]. While MIL variants, especially attention-based MIL (AttMIL) [20], have succeeded in diagnostic tasks, they struggle with complex prognostic challenges like recurrence prediction. This limitation primarily stems from their patch-level operations, which fail to capture intricate spatial relationships, contextual dependencies, and, crucially, the explicit modeling of individual cells, their phenotypes, and the dynamic ecological relationships within the tumor microenvironment that are essential for understanding recurrence risk.

Advanced MIL approaches have attempted to address some of these limitations through architectural innovations. Clustering-Constrained Attention MIL (CLAM) [21] integrates attention with instance-level clustering for coherent feature representations within morphologically consistent regions. Transformer-Based MIL (TransMIL) [22] employs Transformer architecture with 2D positional encoding to better capture spatial correlations between tissue patches. Cross-Attention-Based Salient Instance Inference MIL (CASiiMIL) [23] uses cross-attention mechanisms to identify rare abnormal regions in highly imbalanced datasets, while Channel Attention-Based MIL (CAMIL) [24] focuses on intra-channel dependencies to highlight discriminative feature dimensions. Recent computational approaches to invasive lung adenocarcinoma recurrence prediction include Kim et al. [34], who achieved an AUC of 0.763 using EfficientNet-B2 within a MIL framework, and Su et al. [35], who developed DAMIL achieving 0.649 AUROC for 5-year recurrence prediction.

Despite these architectural advances, a fundamental limitation persists across all existing MIL methods: they operate on predefined tissue patches without explicit modeling of individual cellular components or their ecological relationships. None directly analyze the behavior of specific cell populations (tumor cells, immune cells, stromal cells), their spatial interactions, or the dynamic microenvironmental contexts that drive disease progression and recurrence. This represents a critical gap, as recurrence risk is ultimately determined by cellular-level processes—immune evasion, epithelial-mesenchymal transition, angiogenesis, and stromal remodeling—that

require explicit cellular modeling to be fully understood and accurately predicted. While cell-level analysis tools like HoVer-Net [25] for nuclear segmentation and classification, and CellViT [26] and CellViT++ [27] for transformer-based cell-level tasks have advanced the field, their integration with prognostic modeling for recurrence prediction remains largely unexplored, representing a significant missed opportunity to harness the full potential of cellular-level information.

To address this fundamental gap, CellEcoNet operationalizes the "language of pathology" paradigm introduced in our framework, where individual cells function as words, their spatial arrangements form phrases, and tissue architecture constitutes sentences. Just as natural language processing models use contextual embeddings to capture how word meanings shift based on surrounding context, CellEcoNet employs spatially aware attention mechanisms to learn how cellular significance varies with microenvironmental context. This biological language exhibits its own grammar: spatial proximity rules govern cell-cell interactions, morphological patterns encode functional states, and architectural arrangements convey prognostic information. The following technical implementation translates these conceptual foundations into a computational framework that can automatically learn and interpret this cellular language for recurrence prediction.

## **2.1 Dataset**

Our study utilized a cohort of 189 patients diagnosed with stage I to III ILA, who underwent curative-intent surgical resection at Wake Forest Baptist Comprehensive Cancer Center between 2008 to 2015. All patients were followed up for a minimum of five years. The cohort included 456 H&E-stained WSIs, with a median of two slides per patient. Patient follow-up data included recurrence status and time to recurrence, with 72 patients (38.1%) experiencing recurrence within five years. The study design diagram (Figure 1 A) outlines the exclusion criteria and study population, while cohort demographics (Figure 1 B) show a balanced distribution of age and race, with slightly more females (56.6%) than males (40.7%), and the sex of 5 patients (2.6%) unknown. Notably, patients who experienced recurrence had higher rates of lymphovascular invasion (29.2% vs. 7.7%) and higher-grade tumors (84.7% vs. 43.6% for Grade 3 in the new grading system, WHO 5<sup>th</sup> Ed. [2021]).

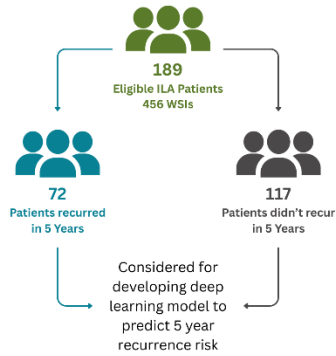
**A**

**Inclusion Criteria:**

- >18 years old
- Histologically confirmed Stage I-III ILA
- Underwent surgical resection at WFBCCC between 2008 to 2015
- 5-Year follow-up data available

**Exclusion Criteria:**

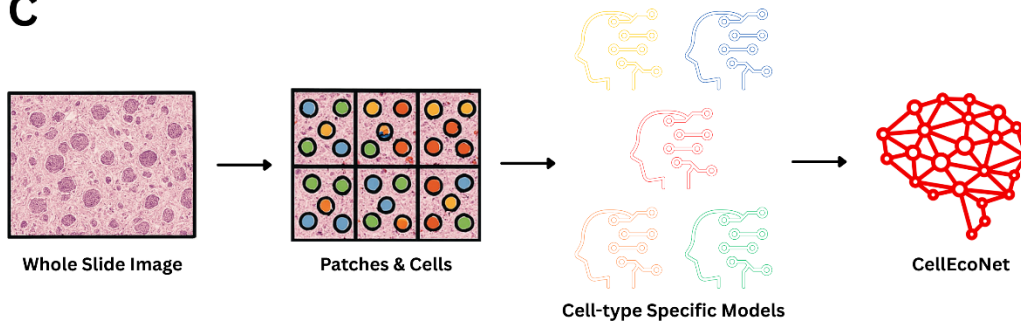
- With previous lung cancer
- With other cancers or serious diseases
- Mucinous adenocarcinoma
- Lost follow-up in 5 years



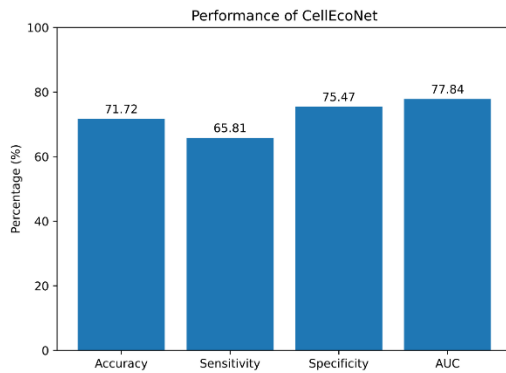
**B**

Characteristic	All (n=189)	No recurrence (n=117)	Recurrence (n=72)
<b>Age at diagnosis</b>			
Median (min, max)	63.3 (39.0, 88.0)	63.0 (43.0, 88.0)	65.5 (39.0, 84.0)
<b>Race</b>			
African American	20 (10.6%)	12 (10.3%)	8 (11.1%)
American Indian or Alaska Native	6 (3.2%)	3 (2.6%)	3 (4.2%)
Asian	1 (0.5%)	1 (0.9%)	0 (0.0%)
Black	3 (1.6%)	3 (2.6%)	0 (0.0%)
Hispanic	3 (1.6%)	2 (1.7%)	1 (1.4%)
Native Hawaiian or Other Pacific Islander	1 (0.5%)	1 (0.9%)	0 (0.0%)
Other	6 (3.2%)	3 (2.6%)	3 (4.2%)
White	149 (78.8%)	92 (78.6%)	57 (79.2%)
<b>Sex</b>			
Female	107 (56.6%)	76 (65.0%)	31 (43.1%)
Male	77 (40.7%)	38 (32.5%)	39 (54.2%)
<b>Death</b>			
Dead	44 (23.3%)	1 (0.9%)	43 (59.7%)
Alive	145 (76.7%)	116 (99.1%)	29 (40.3%)
<b>Survival (month)</b>			
Median (min, max)	60.0 (4.0, 60.0)	60.0 (25.0, 60.0)	47.0 (4.0, 60.0)
<b>AJCC Stage</b>			
Median (min, max)	2.0 (1.0, 7.0)	1.0 (1.0, 7.0)	2.0 (1.0, 6.0)
<b>Predominant Pattern-Based Grade</b>			
Grade 1	57 (30.2%)	47 (40.2%)	10 (13.9%)
Grade 2	102 (54.0%)	54 (46.2%)	48 (66.7%)
Grade 3	30 (15.9%)	16 (13.7%)	14 (19.4%)
<b>IASLC Grade</b>			
Grade 1	24 (12.7%)	23 (19.7%)	1 (1.4%)
Grade 2	53 (28.0%)	43 (36.8%)	10 (13.9%)
Grade 3	112 (59.3%)	51 (43.6%)	61 (84.7%)
<b>Intratumoral lymphocytes</b>			
Present	92 (48.7%)	58 (49.6%)	34 (47.2%)
Absent	97 (51.3%)	59 (50.4%)	38 (52.8%)
<b>Lymphovascular invasion</b>			
Absent	159 (84.1%)	108 (92.3%)	51 (70.8%)
Present	30 (15.9%)	9 (7.7%)	21 (29.2%)

**C**



**D**



**E**

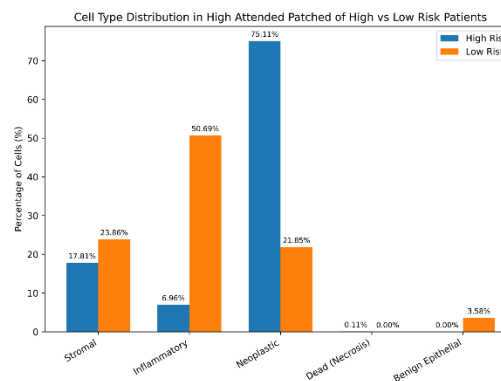
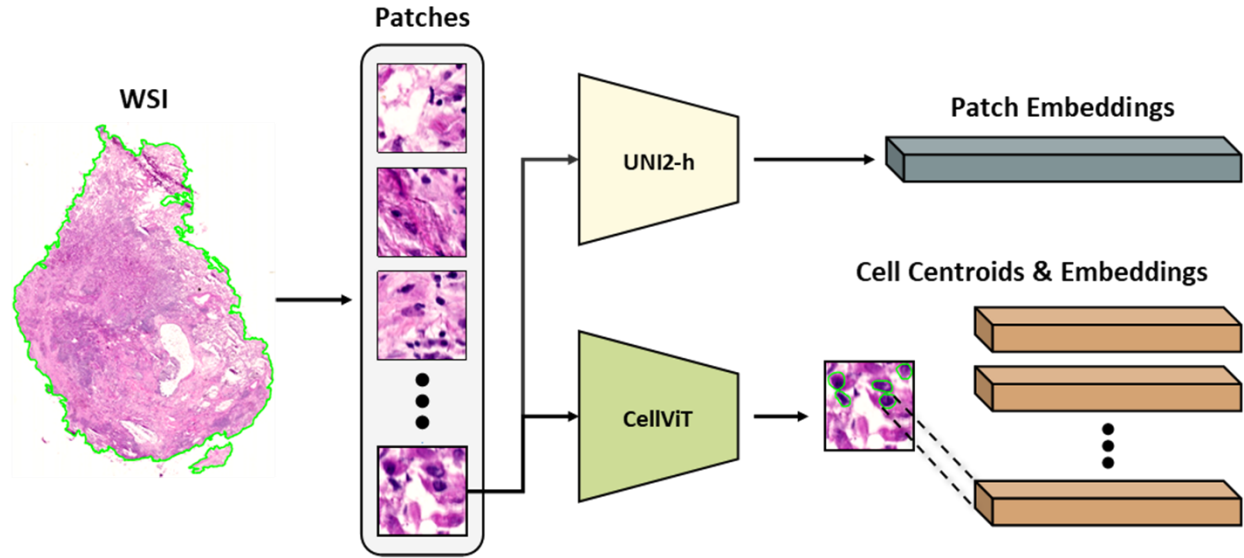


**Figure 1:** (A) Study population characteristics and cohort design. This shows patient selection criteria for invasive lung adenocarcinoma cases from 2008-2015, including exclusion criteria (previous lung cancer; other cancers or serious diseases (life-threatening conditions), mucinous adenocarcinoma, and lost follow-up within 5 years). The final study population comprised 189 patients with 456 whole slide images, stratified into recurrence (patients = 72, WSIs = 170) and non-recurrence (patients = 117, WSIs = 286) groups based on 5-year follow-up data. (B) Demographic and clinical characteristics of patients with invasive lung adenocarcinoma examined in this study. Data are presented for the entire cohort (n=189) and stratified by recurrence status (no recurrence, n=117; recurrence, n=72). Variables include age at diagnosis, race, sex, survival outcomes, AJCC stage, histological grade (old and new classification systems), intratumoral lymphocytes, and lymphovascular invasion status. (C) Overall idea of the deep learning pipeline proposed in this study. (D) Bar chart showing the performance of CellEcoNet across different metrics. (E) Cell type distribution in the highly attended patched of correctly predicted high vs low risk patients.

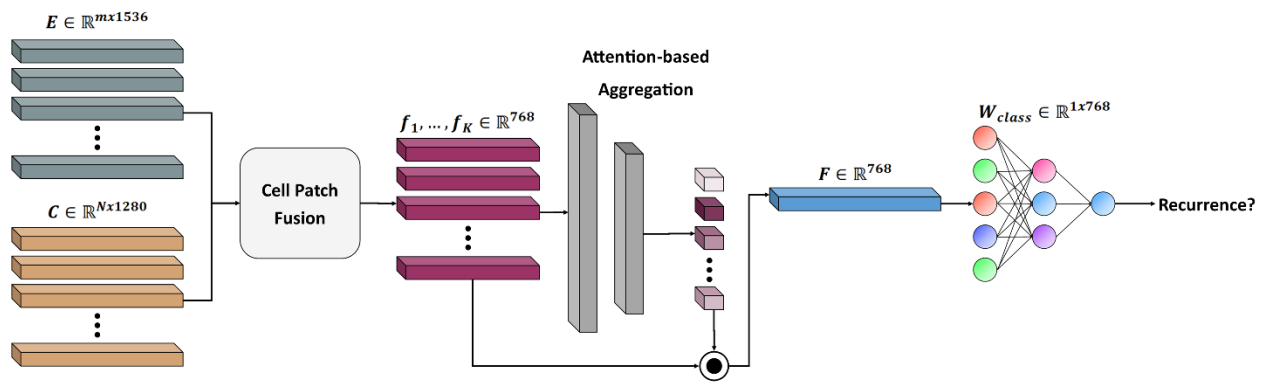
## 2.2 Overview of CellEcoNet Framework

We propose CellEcoNet, a novel multi-scale DL framework to predict 5-year recurrence in ILA from H&E-stained WSIs. CellEcoNet implements the "language of pathology" concept through three core components that mirror natural language processing architectures: (1) multi-scale feature extraction captures both "words" (individual cells at 40 $\times$ ) and "sentences" (tissue patches at 20 $\times$ ), (2) cell-to-patch mapping and fusion creates contextual embeddings by linking cellular "words" with their architectural "sentences," and (3) multi-dimensional attention mechanisms learn complex semantic relationships between tissue regions, analogous to how transformers capture dependencies between sentence elements. This architecture addresses the fundamental limitations of current computational pathology methods by integrating information across multiple scales and explicitly modeling cellular and intercellular characteristics within their biological context. Figure 2 illustrates the overall architecture of CellEcoNet.

## A. Multi-Scale Feature Extraction



## B. Overview of CellEcoNet



## C. Cell Patch Fusion

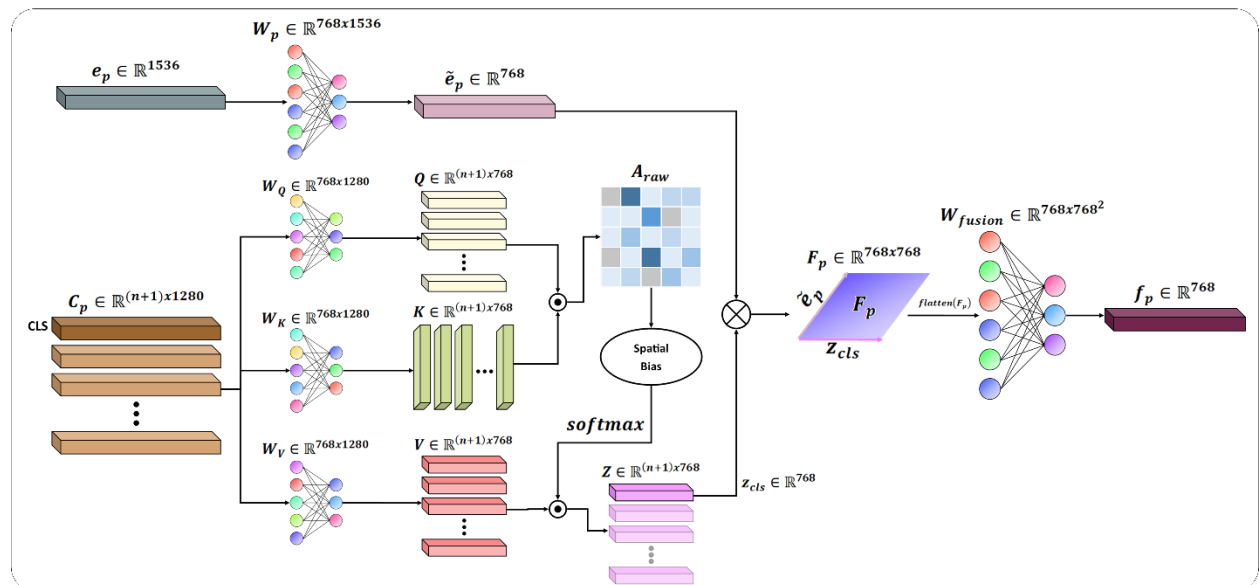


**Figure 2:** Overview of the CellEcoNet for invasive lung adenocarcinoma (ILA) recurrence prediction. (A) Whole slide image (WSI) processing pipeline showing dual-scale feature extraction at 20× (tissue patches) and 40× (individual cells). (B) Multi-dimensional attention projection that extends traditional 1D attention to 2D space for improved discriminative power. (C) Patch-cell fusion module that integrates cellular and tissue-level information through self-attention and outer product operations.

Each component is designed to address specific gaps identified in existing methods while maintaining the conceptual coherence of treating pathology images as a structured biological language that can be computationally parsed and interpreted, as detailed in the following sections.

## 2.3 Multi-Scale Feature Extraction

Our multi-scale feature extraction strategy implements the core principle of the pathology language: cells at 40× magnification serve as the fundamental "words" encoding fine-grained morphological and phenotypic information, while tissue patches at 20× magnification represent "sentences" that provide architectural context and spatial organization. This dual-scale approach mirrors how language models require both token-level understanding (individual word meanings) and sequence-level comprehension (sentence structure and context) to achieve semantic understanding. Just as word embeddings capture lexical information while sentence embeddings capture syntactic and semantic relationships, our cellular embeddings encode morphological details while patch embeddings capture tissue architecture and spatial patterns.

As illustrated in Figure 2(A), we adopted a two-step feature extraction strategy:

- **Patch-Level Feature Extraction (20x):** WSIs were tiled into non-overlapping 256x256 pixel patches at 20x magnification. Using a pre-trained foundation model, UNI2-h [36], we extracted a feature vector  $e_p \in \mathbb{R}^{1536}$  for each patch  $p$ , capturing broad morphological and tissue-architectural patterns. We used Trident [37, 38] for tissue segmentation, patch cropping, and feature extraction.
- **Cell-Level Feature Extraction (40x):** Concurrently, cell nuclei were segmented and classified from WSIs at 40× magnification using CellViT++ [26, 27], specifically the SAM-based model [39]. This model yields embeddings  $c_i \in \mathbb{R}^{1280}$  for each individual cell  $c_i$ , encoding fine-grained morphological and phenotypic details across five major cell categories: stromal, inflammatory, neoplastic, dead, and benign epithelial. It also outputs centroid coordinates for each cell. Preprocessing was performed using PathoPatcher [40].

This dual-scale approach (20x for summarizing path level information and 40x for capturing subtle information at cell level) overcomes the limitations of single-scale modeling, enabling the simultaneous utilization of both cellular morphology and tissue architecture.

## 2.4 Cell-to-Patch Mapping and Spatially Biased Cell Attention

The integration of cellular and tissue-level information implements contextual embedding principles from natural language processing, where the meaning of individual elements depends critically on their surrounding context. In CellEcoNet, a cell's biological significance—much like

a word's semantic meaning—is determined not only by its intrinsic morphological features but also by its spatial neighbors and architectural context. The spatially biased attention mechanism we introduce mimics how attention mechanisms in language models allow words to attend to relevant context, enabling our framework to automatically learn which cellular neighborhoods are most informative for recurrence prediction.

### 2.4.1 Cell-to-Patch Mapping

We established a spatial correspondence between cells and patches by mapping each cell to the patch containing its centroid. Formally, for each patch  $p$ , we define the set of corresponding cells as:

$$C_p = \{c_i \in C | \text{centroid}(c_i) \in p\},$$

where  $C_p$  is the set of cells whose centroids lie within the spatial bounds of patch  $p$ , and  $C$  is the full set of cells. This mapping preserves spatial context, linking cells to the patch that contains them.

### 2.4.2 Spatially Biased Cell Self-Attention

Each patch embedding  $e_p \in \mathbb{R}^{1536}$ , was linearly projected to  $\mathbb{R}^{768}$  via a learned projection:

$$\tilde{e}_p = W_p e_p, \text{ where } W_p \in \mathbb{R}^{768 \times 1536}$$

Each patch  $p$  contains  $c$  cells, we denote the cell embeddings as  $c_1, c_2, c_3, \dots, c_c \in \mathbb{R}^{1280}$ . Each  $c_i$  is passed through LayerNorm both before and after attention. We aggregate these variable-length cell embeddings using a self-attention mechanism with a learnable CLS token  $e_{CLS} \in \mathbb{R}^{1280}$ . The input sequence is:

$$C_p = [e_{CLS}, c_1, \dots, c_c] \in \mathbb{R}^{(n+1) \times 1280}$$

We apply learned projections:

$$Q = W_Q \cdot X, \quad K = W_K \cdot X, \quad V = W_V \cdot X,$$

where  $W_Q, W_K, W_V \in \mathbb{R}^{768 \times 1280}$ .

We computed the raw attention scores between all elements:

$$A_{raw} = \frac{(Q \cdot K^T)}{\sqrt{d_K}},$$

where  $d_K$  is the dimension of the key vectors i.e., 768. Then, we incorporated spatial information by subtracting the physical distance between cell centroids from the attention scores:

$$A_{spatial(i,j)} = A_{raw(i,j)} - \text{dist}(\text{centroid}_i, \text{centroid}_j),$$

where  $dist(\cdot, \cdot)$  is the Euclidean distance between cell centroids. This spatial bias implements the grammatical rules of pathology language, where cellular proximity defines semantic relationships—just as word order and adjacency create meaning in natural language, spatial arrangements of cells encode biological function and prognostic significance. Cells in close proximity form functional neighborhoods that act as coherent semantic units within the tissue microenvironment. This enables the framework to capture local cellular neighborhoods and their collective behavior, which is crucial for understanding TME characteristics and their role in cancer progression. We then applied softmax normalization to obtain the final attention weights:

$$A = \text{softmax}(A_{\text{spatial}})$$

The output of the self-attention layer is computed by:

$$Z = A \cdot V$$

The updated CLS token  $z_{CLS} \in \mathbb{R}^{768}$  is extracted from the first row of  $Z$ , which now contains aggregated information from all cells within the patch, with greater influence from spatially proximal cells.

This spatially biased self-attention mechanism allows the framework to selectively focus on informative cells while capturing cell-cell interactions within each patch, addressing the homogeneous treatment of cells in current approaches.

## 2.5 Cross-Scale Fusion

Cross-scale fusion represents the critical step where "word-level" cellular information is integrated with "sentence-level" tissue architecture, analogous to how transformer models combine token embeddings with positional and contextual information. This fusion captures the biological reality that cellular behavior cannot be understood in isolation—just as word meaning depends on sentence context, cellular significance emerges from the interplay between intrinsic cell properties and their tissue microenvironment. The outer product operation we employ creates a rich representation space that captures all possible interactions between cellular morphology and architectural context, as illustrated in Figure 2(C).

For each patch  $p$ , we have a patch embedding vector  $\tilde{e}_p \in \mathbb{R}^{768}$  and an aggregated cell embedding vector  $z_{CLS} \in \mathbb{R}^{768}$ , we computed the outer product between these vectors:

$$F_p = \tilde{e}_p \otimes z_{CLS} \in \mathbb{R}^{768 \times 768}$$

This matrix captures all pairwise multiplicative interactions between patch and cell features. To make this representation computationally tractable, we flattened the matrix and projected it back to 768 dimensions using a learnable projection matrix  $W_{\text{fusion}}$ :

$$f_p = W_{\text{fusion}} \cdot \text{flatten}(F_p), \quad W_{\text{fusion}} \in \mathbb{R}^{768 \times 768^2}$$

where  $f_p \in \mathbb{R}^{768}$  is the final fused representation for patch  $p$ .

This fusion mechanism enables rich cross-scale interactions that would be missed by simpler concatenation or addition operations, allowing the framework to capture how cellular characteristics interact with tissue architecture to influence recurrence risk.

## 2.6 Multi-Dimensional Attention MIL

The fused embeddings  $f_1, \dots, f_K \in \mathbb{R}^{768}$  from a WSI form a "bag" of  $K$  instances. We employed AttMIL to aggregate these instance features into a slide-level representation for predicting recurrence. This concept is visualized in Figure 2(B).

### 2.6.1 Conventional 1D Attention (AttMIL)

As a baseline and part of our ablation, we used the standard AttMIL, where instance embeddings  $h_k$  (our  $f_k$ ) are projected onto a 1D space, see the equation below for reference, to get attention weights  $\alpha_k$ , which are then used to compute a weighted sum of instance embeddings.

$$\alpha_k = \frac{\exp \{w^T (\tanh(Vh_k^T) \odot \text{sigmoid}(Uh_k^T))\}}{\sum_{j=1}^K \exp \{w^T (\tanh(Vh_j^T) \odot \text{sigmoid}(Uh_j^T))\}}$$

where  $V, U$  are learnable subspaces, and  $\odot$  denotes element-wise multiplication. The scalar  $w^T(\cdot)$  collapses the transformed instances into a single attention score. The reliance on a single weight vector  $w$  can produce identical attention scores for instances with divergent feature interactions when projected onto the 1D subspace defined by  $w$ .

### 2.6.2 Novel 2D and 3D Attention Projections:

To overcome the limitations of 1D projection, we extended this by projecting  $h_k$  onto a 2D or 3D plane/space using two ( $w_1, w_2$ ) or three ( $w_1, w_2, w_3$ ) learnable weight vectors, respectively. This can be written mathematically as:

$$\alpha_k = \frac{\exp \{ \left\| W^T (\tanh(Vh_k^T) \odot \text{sigmoid}(Uh_k^T)) \right\|_F \}}{\sum_{j=1}^K \exp \{ \left\| W^T (\tanh(Vh_j^T) \odot \text{sigmoid}(Uh_j^T)) \right\|_F \}}$$

where  $\|\cdot\|_F$  is the Frobenius norm. This allows the framework to assign importance based on a richer, multi-faceted representation of each instance.

## 2.7 Cell-Type Specific Models

Cell-type-specific modeling reflects the concept that different cellular populations represent distinct "vocabularies" within the pathology language, each with specialized semantic roles in the tumor microenvironment. Just as domain-specific language models excel in specialized contexts (medical texts, legal documents, scientific literature), our cell-type-specific models become experts in interpreting the unique contributions of different cellular populations to recurrence

risk. The ensemble approach combines these specialized "linguistic perspectives," recognizing that comprehensive understanding of tissue biology—like natural language comprehension—benefits from integrating multiple specialized knowledge domains.

Let the five major cell types be denoted by the set:

$$T = \{\textit{stromal}, \textit{inflammatory}, \textit{neoplastic}, \textit{dead}, \textit{benign epithelial}\}$$

### 2.7.1 Cell-Type Specific Subsets

For each cell type  $t \in T$ , we constructed a subset of each WSI as follows:

Let  $C_t \subseteq C$  be the set of all cells of type  $t$  present in a WSI.

Using the spatial mapping dictionary (Section 2.4.2), we selected the set of patches  $P_t \subseteq P$ , where each patch  $p \in P_t$  satisfies:

$$C_p \cap C_t \neq \emptyset,$$

meaning the patch contains at least one cell of type  $t$ .

Each model  $M_t$  was then trained using the subset  $S_t = \{P_t, C_t\}$ , resulting in five specialized models focused on learning the recurrence-related patterns associated with a specific cell type.

A sixth model, denoted  $M_{all}$ , was trained using all cell embeddings and all patches that contained at least one cell of any type:

$$P_{all} = \{p \in P | C_p \neq \emptyset\}$$

This model captures holistic cellular heterogeneity and serves as a comprehensive multi-cell-type baseline.

### 2.7.2 Ensemble Integration via Patient-Level Majority Voting

To integrate predictions across cell-type-specific perspectives, we employed a patient-level ensemble approach based on majority voting.

Let a patient  $i$  have  $S_i$  WSIs, and let  $M = \{M_1, M_2, \dots, M_6\}$  be the six trained models (five cell-type-specific and one multi-type model). Each model  $M_m \in M$  outputs a probability score  $p_{i,s}^{(m)} \in [0, 1]$  for slide  $s \in \{1, \dots, S_i\}$  of patient  $i$ .

The aggregated patient-level probability for model  $M_m$  is computed as the average over all WSIs:

$$\tilde{p}_i^{(m)} = \frac{1}{S_i} \sum_{s=1}^{S_i} p_{i,s}^{(m)}$$

The final patient-level prediction is then obtained by averaging the probabilities across all models:

$$\tilde{p}_i = \frac{1}{|M_i|} \sum_{m \in M_i} \tilde{p}_i^{(m)},$$

where  $M_i \subseteq M$  includes only the models applicable to patient  $i$  (i.e., for which at least one relevant cell is found).

The final binary decision is made using a threshold  $\tau \in [0,1]$  ( $\tau = 0.5$ ):

$$\hat{y}_i = \begin{cases} 1, & \text{if } \tilde{p}_i \geq \tau \\ 0, & \text{otherwise} \end{cases}$$

This ensemble strategy leverages the distinct predictive power of each cell type while combining them to improve generalizability and robustness. It also reflects the biological heterogeneity of the TME, where different cell populations contribute uniquely to tumor progression and recurrence.

## 3 Results

We evaluated the performance of our CellEcoNet framework for predicting 5-year recurrence in ILA patients using a dataset of 456 H&E-stained slides from 189 patients. Our framework leverages both patch-level (20 $\times$ ) and cell-level (40 $\times$ ) information through a novel patch-cell fusion mechanism with 2D attention projection. All experiments were conducted using 5-fold cross-validation, with consistent folds across all methods except DAMIL.

### 3.1 Comparison with Clinical Baselines

To establish a clinical baseline, we evaluated the predictive performance of established clinicopathologic grading and staging systems for 5-year recurrence risk. For AUC calculation, we trained separate logistic regression models using each system as the sole predictor, with model performance assessed on a held-out test set. For time-to-event analysis, we fitted univariable Cox proportional hazards models to estimate hazard ratios (HR) with 95% confidence intervals (CI) and calculated concordance indices (C-index). The dominant pattern-based grading system achieved an AUC of 0.648, HR of 2.02 (95% CI: 1.41–2.89), and C-index of 0.630; the IASLC grading system achieved an AUC of 0.714, HR of 2.36 (95% CI: 1.91–2.91), and C-index of 0.672; and the AJCC stage achieved an AUC of 0.640, HR of 1.17 (95% CI: 1.08–1.28), and C-index of 0.636.

### 3.2 Comparison with State-of-the-Art Methods

We compared CellEcoNet with several state-of-the-art methods for computational pathology, including AttMIL, CLAM, TransMIL, and DAMIL. As shown in Figure 3, our Combined model outperformed all competing methods across key performance metrics. CellEcoNet achieved an

AUC of 77.84%, significantly outperforming all baselines: AttMIL (66.57%), CLAM (66.13%), TransMIL (62.29%), CAMIL (67.47%), DAMIL (64.90%), and Kim et al. (66.81%) [34]. These improvements were consistent across all metrics, with notable gains in sensitivity. The results are visualized in Figure 3 and detailed metric can be found in Table 1.

### 3.2.1 Methodological Considerations

Kim et al. used EfficientNet-b0 fine-tuned on patch-level classification (slide labels assigned to patches) as an encoder, followed by AttMIL. As their model and code was unavailable, we attempted to replicate their encoder training approach but found it ineffective on our dataset. For fairness, we replaced their encoder with UNI2-h in our comparison.

DAMIL (Su et al.) [35] employed CTransPath as their encoder and reported the results on the same dataset as ours but different data folds, making direct comparisons imperfect. We include their results for completeness but note that performance differences may stem from these methodological disparities.

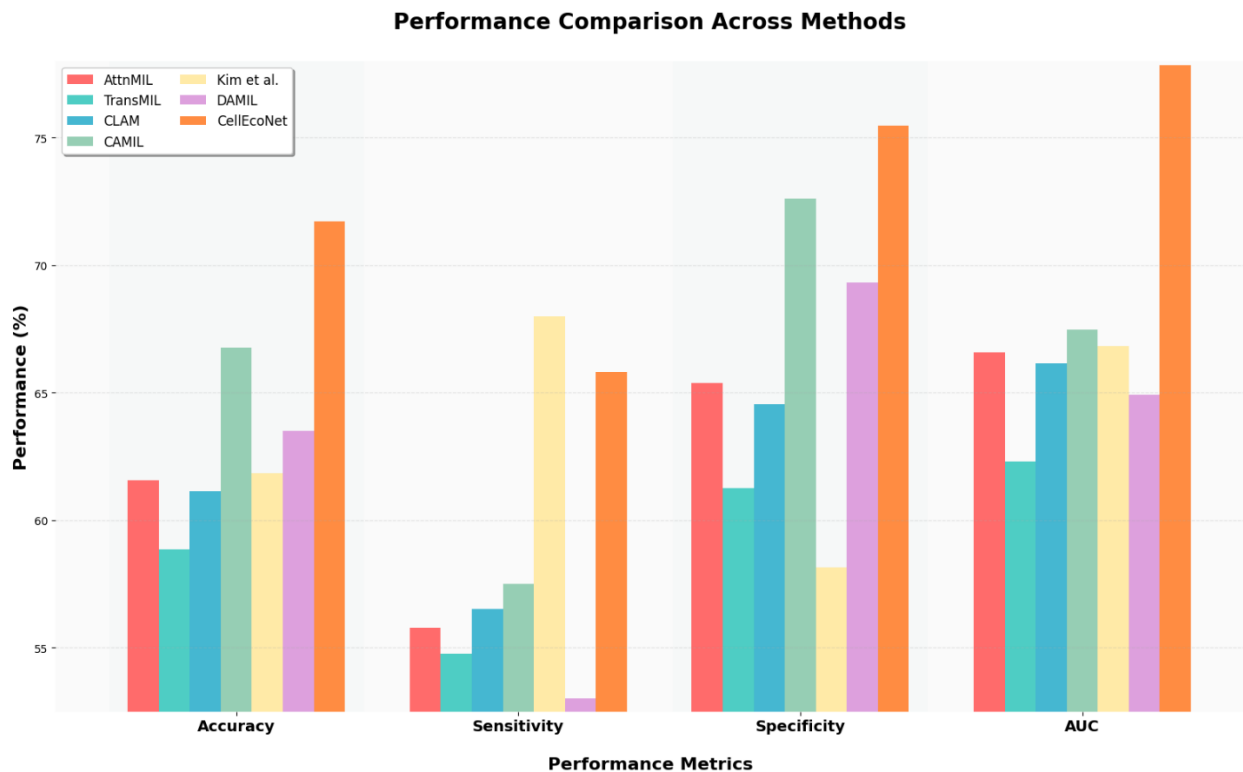


**Figure 3:** Performance comparison between CellEcoNet and state-of-the-art methods. Bar plots showing mean accuracy, sensitivity, specificity, and AUC (with standard deviation across five folds) for AttMIL (red), TransMIL (teal), CLAM (blue), CAMIL (mint), Kim et al. (yellow), DAMIL (lavender), and CellEcoNet (orange). CellEcoNet outperforms all competing methods across all metrics, with particularly notable improvements in accuracy (71.7% vs. next best 66.8%), specificity (75.5% vs. next best 72.6%) and AUC (77.84% vs. next best 67.5%).

**Table 1:** Performance comparison of state-of-the-art MIL methods with our best performing model. Metrics show mean  $\pm$  standard deviation across test folds. \*DAMIL uses a different encoder (CTransPath), and data folds compared to other methods. Best performance in each metric is bolded, while second-best is underlined.

Model	Accuracy (%)	Sensitivity (%)	Specificity (%)	AUC (%)
-------	--------------	-----------------	-----------------	---------

AttMIL	61.55 ± 8.23	55.77 ± 12.04	65.39 ± 7.79	66.57 ± 5.55
TransMIL	58.85 ± 5.14	54.75 ± 5.29	61.26 ± 9.2	62.29 ± 3.85
CLAM	61.13 ± 7.52	56.52 ± 12.89	64.56 ± 12.18	66.13 ± 5.90
CAMIL	<u>66.77 ± 3.75</u>	57.50 ± 7.17	<u>72.60 ± 3.63</u>	<u>67.47 ± 5.70</u>
Kim et al.	61.84 ± 7.18	<b>68.00 ± 11.6</b>	58.16 ± 17.93	66.81 ± 5.54
DAMIL*	63.50 ± 3.10	53.00 ± 7.90	69.30 ± 6.60	64.90 ± 1.20
CellEcoNet (ours)	<b>71.72 ± 4.82</b>	<u>65.81 ± 7.39</u>	<b>75.47 ± 5.38</b>	<b>77.84 ± 3.99</b>

### 3.3 Classification Performance Metrics

We developed separate models for five distinct cell types: stromal cells, inflammatory cells, neoplastic cells, dead cells, and benign epithelial cells. Each cell-type specific model demonstrated strong discriminative ability in distinguishing between patients at high and low risk of recurrence.

The benign epithelial cell model achieved particularly strong performance with an AUC of 74.98%, accuracy of 69.14%, sensitivity of 64.94%, and specificity of 71.24%. The stromal cell model yielded an AUC of 71.69%, accuracy of 63.81%, sensitivity of 62.89%, and specificity of 64.26%, while the inflammatory cell model achieved an AUC of 70.27%, accuracy of 64.12%, sensitivity of 62.09%, and specificity of 65.27%. The neoplastic cell model showed an AUC of 71.92%, accuracy of 65.64%, sensitivity of 63.36%, and specificity of 67.13%, and the dead cell model demonstrated an AUC of 72.99%, accuracy of 67.30%, sensitivity of 64.38%, and specificity of 69.14%.

The All-Cell model, which processes all cell types together without distinguishing between them, achieved an AUC of 74.28%, accuracy of 68.60%, sensitivity of 61.89%, and specificity of 73.32%.

Our Combined model, which integrates predictions from all cell-type specific models through majority voting, demonstrated superior performance with an AUC of 77.8%, accuracy of 71.72%, sensitivity of 65.81%, and specificity of 75.47%. This ensemble approach effectively leverages the complementary information provided by different cell types, resulting in more robust predictions. These results are summarized in Figure 4, and detailed metrics can be found in Table 2.

### Performance Comparison Across Different Cell Populations

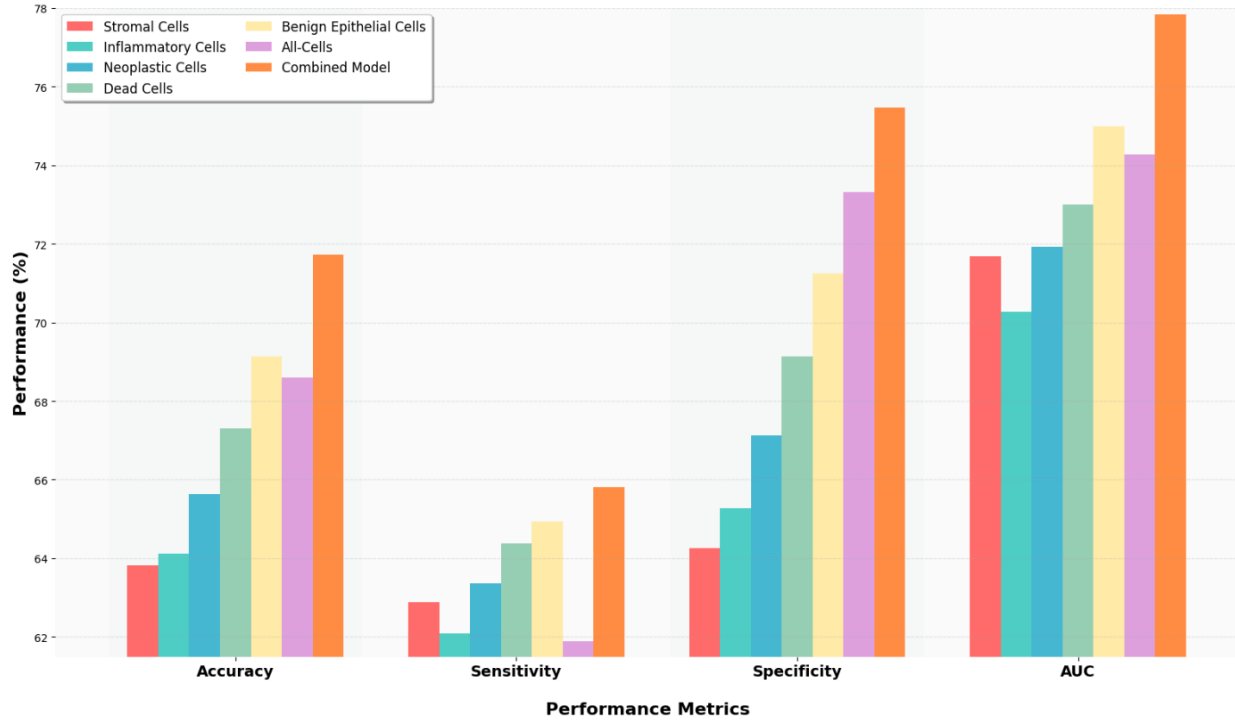


**Figure 4:** Classification performance metrics of cell-type specific and ensemble models for 5-year recurrence prediction. Bar plots showing mean accuracy, sensitivity, specificity, and AUC (with standard deviation across five folds) for each model: Stromal Cell (red), Inflammatory Cell (teal), Neoplastic Cell (blue), Dead Cell (mint), Benign Epithelial Cell (yellow), All-Cells model (lavender), and Combined Ensemble model (orange). The Combined Ensemble model demonstrates superior performance across all metrics, particularly in AUC (77.84%) and balanced sensitivity-specificity.

**Table 2:** Performance comparison of cell-type-specific models, the All-Cells model, and the Combined Model for ILA recurrence prediction. Metrics include accuracy, sensitivity, specificity, and AUC (mean  $\pm$  standard deviation across test folds). The Combined Model (ensemble) achieves the highest performance across all metrics (bold). The second-best results are underlined.

Model	Accuracy (%)	Sensitivity (%)	Specificity (%)	AUC (%)
<b>Stromal Cells</b>	63.81 $\pm$ 4.40	62.89 $\pm$ 7.27	64.26 $\pm$ 7.63	71.69 $\pm$ 6.31
<b>Inflammatory Cells</b>	64.12 $\pm$ 3.50	62.09 $\pm$ 5.50	65.27 $\pm$ 3.84	70.27 $\pm$ 6.49
<b>Neoplastic Cells</b>	65.64 $\pm$ 4.78	63.36 $\pm$ 4.69	67.13 $\pm$ 5.52	71.92 $\pm$ 3.26
<b>Dead Cells</b>	67.30 $\pm$ 1.73	64.38 $\pm$ 10.63	69.14 $\pm$ 7.80	72.99 $\pm$ 3.89
<b>Benign Epithelial Cells</b>	<u>69.14 <math>\pm</math> 2.84</u>	<u>64.94 <math>\pm</math> 4.39</u>	71.24 $\pm$ 4.99	<u>74.98 <math>\pm</math> 3.36</u>
<b>All-Cells</b>	68.60 $\pm$ 1.62	61.89 $\pm$ 6.17	<u>73.32 <math>\pm</math> 5.78</u>	74.28 $\pm$ 3.07
<b>Combined Model</b>	<b>71.72 <math>\pm</math> 4.82</b>	<b>65.81 <math>\pm</math> 7.39</b>	<b>75.47 <math>\pm</math> 5.38</b>	<b>77.84 <math>\pm</math> 3.99</b>

### 3.4 Kaplan-Meier Analysis and Hazard Ratios

To assess clinical utility, we calculated HR for each model using Cox proportional hazards regression. The Combined model achieved the highest HR of 9.54 (95% CI: 4.34–20.98,  $p < 0.005$ ), indicating that patients classified as high-risk by this model had a 9.54-fold higher risk of recurrence compared to those classified as low-risk. This represents a substantial improvement over the All-Cell model (HR: 7.70, 95% CI: 3.80–15.60,  $p < 0.005$ ).

Among the cell-type specific models, the benign epithelial cell model demonstrated the strongest risk stratification capability with an HR of 6.04 (95% CI: 3.15–11.56,  $p < 0.005$ ), followed by the dead cell model (HR: 5.69, 95% CI: 2.96–10.96,  $p < 0.005$ ), stromal cell model (HR: 5.44, 95% CI: 2.69–11.02,  $p < 0.005$ ), inflammatory cell model (HR: 5.06, 95% CI: 2.41–10.62,  $p < 0.005$ ), and neoplastic cell model (HR: 4.98, 95% CI: 2.46–10.06,  $p < 0.005$ ).

The Kaplan-Meier curves visually confirm these findings, showing clear separation between high- and low-risk groups for all models, with All-Cells and Combined model (see Figure 5) demonstrating the most pronounced separations. The HRs for all models with detailed Cox regression results are provided in Table 3.

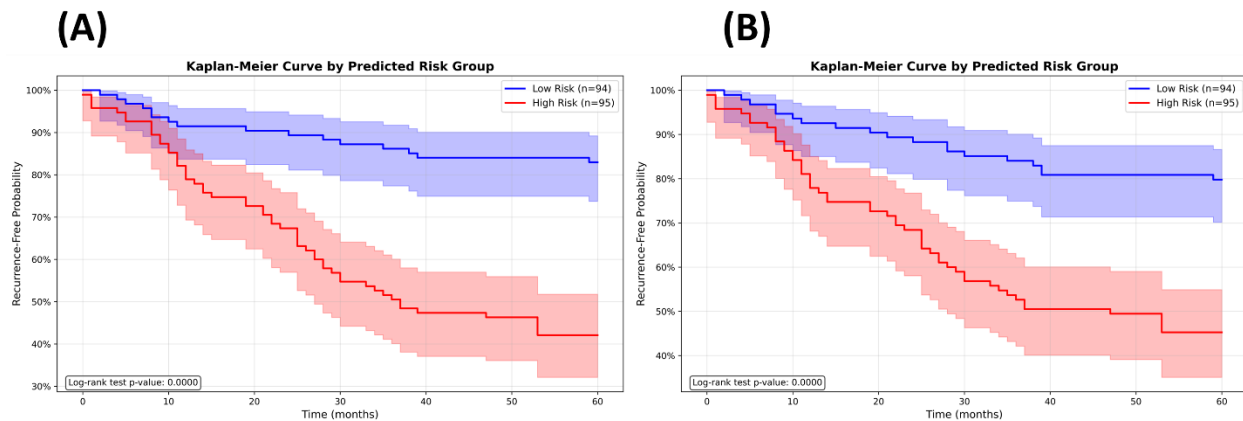


**Figure 5:** Kaplan-Meier (KM) recurrence-free survival curves stratified by predicted risk groups for each model. (A) shows the KM curve of all-cell model and (B) shows the KM curve of the combined model. Each panel shows the survival probability over 60 months for patients classified as low-risk (blue) and high-risk (red) by the respective model, with 95% confidence intervals (shaded areas). All models demonstrate significant stratification ability (log-rank test  $p < 0.0001$ ), with clear separation between risk groups maintained throughout the follow-up period.

### 3.5 Concordance Index Analysis

The concordance index (C-index) measures a model's ability to correctly rank patients according to their recurrence risk. The benign epithelial cell model achieved a mean C-index of  $0.71 \pm 0.02$  across the five folds, indicating its superior ability to rank patients according to their recurrence risk.

The stromal cell model yielded a mean C-index of  $0.67 \pm 0.05$ , while the inflammatory cell model achieved  $0.67 \pm 0.02$ . The neoplastic cell model showed a mean C-index of  $0.66 \pm 0.04$  and the dead cell model demonstrated a mean C-index of  $0.69 \pm 0.02$ .

The All-Cell model achieved a mean C-index of  $0.70 \pm 0.03$ , while our Combined model demonstrated a mean C-index of  $0.70 \pm 0.02$ . These results highlight that each cell type contributes unique prognostic information, with benign epithelial and dead cells providing the most consistent predictive value across folds. A summary of C-index performance across all models is presented in Table 3.

**Table 3:** HR and C-Index of all models including cell-type specific, all-cell and combined models. The table also shows the 95% confidence interval of the HRs with a  $p$ -value  $< 0.005$ , as well as the standard deviation of C-Index across folds.

Model	HR	C-Index
Stromal Cell	5.44 [2.69–11.02]	0.671 $\pm$ 0.05
Inflammatory Cell	5.06 [2.41–10.62]	0.666 $\pm$ 0.02
Neoplastic Cell	4.98 [2.46–10.06]	0.663 $\pm$ 0.04
Dead Cell	5.69 [2.96–10.96]	0.688 $\pm$ 0.02
Benign Epithelial Cell	6.04 [3.15–11.56]	<b>0.708 <math>\pm</math> 0.02</b>
All-Cells	<u>7.70 [3.80–15.60]</u>	0.698 $\pm$ 0.03
Combined Model	<b>9.54 [4.34–20.98]</b>	<u>0.704 <math>\pm</math> 0.02</u>

### 3.6 Optimization for Clinical Utility

To enhance clinical significance, we introduced a novel stopping criterion that balances sensitivity and specificity during model training. The criterion is formulated as:

$$Score = (Sensitivity + Specificity) - |Sensitivity - Specificity|$$

which prioritizes models with harmonized performance across both metrics, avoiding biases toward overly sensitive or specific predictions. All models (including baseline comparisons) were trained using early stopping on the validation set based on this score, and test-set metrics for the optimal validation epoch are reported in Tables 2 and 3. This approach ensures fairness in comparisons while aligning model selection with clinical needs, where trade-offs between false positives and negatives are critical.

### 3.7 Ablation Study

To rigorously evaluate the contributions of different components in our framework, we conducted a comprehensive ablation study across various configurations: 1D Projection (baseline), 2D Projection, 3D Projection, 1D without patch embeddings, and 2D without patch embeddings. These configurations test different aspects of our architecture: 1D, 2D, and 3D Projection variants modify the dimensionality of the attention mechanism (projecting instance features onto 1-dimensional, 2-dimensional, or 3-dimensional spaces for attention weight calculation), while the "without patch embeddings" variants remove tissue-level context by using only cell-level information without the corresponding patch-level features from the same spatial regions. Performance was assessed using accuracy, sensitivity, specificity, and AUC on both validation and test sets.

#### 3.7.1 Validation Performance Comparison

The 1D Projection (baseline) achieved a mean validation AUC of  $67.63 \pm 3.34$ , with sensitivity and specificity at  $59.92 \pm 2.91$  and  $63.92 \pm 4.74$ , respectively. The 2D Projection demonstrated significant improvements, achieving a 3.6% higher mean validation AUC ( $70.06 \pm 1.95$ ) than the baseline. Notably, the 2D variant improved sensitivity by 12.7% ( $67.55 \pm 7.37$  vs.  $59.92 \pm 2.91$ ), confirming its ability to better model feature interactions through orthogonal attention

mechanisms. Expanding to 3D Projection did not yield further gains; instead, validation AUC dropped by 3.3% ( $67.61 \pm 6.93$ ) compared to 2D, with sensitivity and specificity variance spiking ( $> \pm 10.01$  std), indicating overparameterization and training instability.

The most severe degradation occurred when patch embeddings were removed. The 1D variant without patches collapsed to a 15.3% lower validation AUC ( $57.31 \pm 3.83$ ) than the baseline, while the 2D variant preserved marginally better performance ( $62.08 \pm 4.83$  AUC), still 8.4% worse than standard 2D. This underscores that patch embeddings contribute critically to model performance, meaning that they capture some complementary information to the cell-level representations.

### 3.7.2 Test Set Confirmation

Test results mirrored validation trends: 2D Projection achieved the highest mean AUC ( $74.28 \pm 3.07$ ), outperforming 1D by 4.9% ( $70.84 \pm 2.48$ ) and 3D by 3.9% ( $71.50 \pm 2.00$ ). Specificity stability also improved (2D std:  $\pm 5.78$  vs. 1D:  $\pm 6.38$ ), reinforcing its robustness. Removing patch embeddings consistently degraded test metrics, validating our design choice to retain them.

The final model (2D attention with patch embeddings) was selected based on validation metrics, with test results and cell-specific analyses further corroborating its advantage, see Table 4 for detailed results. This systematic evaluation ensures that our design decisions are empirically grounded, maximizing both discriminative power and robustness.

**Table 4:** Performance comparison across ablation settings, showing validation and test results (mean  $\pm$  std) for models with different projection dimensions (1D, 2D, 3D) and patch embedding configurations. Bold values highlight top-performing configurations per metric, while the underlined show the second best. P.E. denotes patch embeddings, A.P. denotes attention projection, Acc stands for accuracy, Sen for sensitivity, and Spe for specificity.

Ablation Settings		Validation Results				Test Results			
P.E.	A.P.	Accuracy	Sensitivity	Specificity	AUC	Accuracy	Sensitivity	Specificity	AUC
✓	1D	<u>62.38<math>\pm</math>4.03</u>	59.91 $\pm$ 2.91	<u>63.90<math>\pm</math>4.74</u>	67.63 $\pm$ 3.34	<u>65.46<math>\pm</math>3.21</u>	<b>67.30<math>\pm</math>5.51</b>	63.90 $\pm$ 6.38	70.83 $\pm$ 2.48
✓	2D	<b>65.74<math>\pm</math>3.22</b>	<u>67.55<math>\pm</math>7.37</u>	<b>64.34<math>\pm</math>6.94</b>	<b>70.06<math>\pm</math>1.95</b>	<b>68.60<math>\pm</math>1.62</b>	61.89 $\pm$ 6.17	<b>73.32<math>\pm</math>5.78</b>	<b>74.28<math>\pm</math>3.07</b>
✓	3D	62.08 $\pm$ 8.04	<b>67.68<math>\pm</math>10.01</b>	58.52 $\pm$ 10.25	67.61 $\pm$ 6.93	64.16 $\pm$ 2.30	<u>66.94<math>\pm</math>8.37</u>	62.25 $\pm$ 9.16	<u>71.50<math>\pm</math>2.00</u>
✗	1D	57.60 $\pm$ 5.54	54.60 $\pm$ 7.64	59.37 $\pm$ 5.25	57.30 $\pm$ 3.83	61.18 $\pm$ 0.85	55.75 $\pm$ 3.56	<u>64.89<math>\pm</math>3.67</u>	63.52 $\pm$ 2.26
✗	2D	58.53 $\pm$ 5.38	65.15 $\pm$ 12.7	54.07 $\pm$ 7.29	62.07 $\pm$ 4.83	61.58 $\pm$ 3.61	64.34 $\pm$ 5.59	59.90 $\pm$ 3.93	64.28 $\pm$ 5.27

## 3.8 Statistical Analysis of Model Bias and Failure Patterns

We conducted a statistical analysis to evaluate whether the model exhibited any unintended biases or consistent failure patterns based on patient demographics or clinical timelines. Model failure was defined as false negatives, cases where a patient experienced recurrence, but the model incorrectly predicted them as low risk.

### 3.8.1 Bias Across Demographic Groups

**Sex Bias:** We compared false negative rates between females and males using a chi-square test. Females had a false negative rate of 11.21%, while males had a rate of 15.58%. The difference was not statistically significant ( $p = 0.5181$ ), indicating no evidence of sex-based model bias.

**Race Bias:** False negative rates were also similar between White (12.75%) and African American (10.00%) patients. A chi-square test returned a p-value of 1.0000, suggesting no racial bias in model predictions.

**Age Group Bias:** Patients were split into two groups based on the median age of 65 years. The false negative rate for older patients was 14.13% compared to 12.37% for younger patients. This difference was not statistically significant ( $p = 0.8870$ ), indicating no age-related bias.

### 3.8.2 Failure Patterns Based on Recurrence Timing

**Recurrence Between 40–59 Months:** We tested whether CellEcoNet failed more frequently in patients who experienced recurrence late in the follow-up period (40–59 months). These patients had a false negative rate of 33.33%, slightly lower than 35.38% for patients who recurred earlier. The difference was not statistically significant ( $p = 0.9198$ ), suggesting no unique failure trend in late recurrence cases.

**Early Recurrence with Early Death:** Patients who recurred within 24 months and died within 60 months had a false negative rate of 41.67%, compared to 33.90% for other recurred patients. While this 10.43% difference is notable, it was not statistically significant ( $p = 0.3659$ ). This may suggest a possible trend toward underprediction in more aggressive cases.

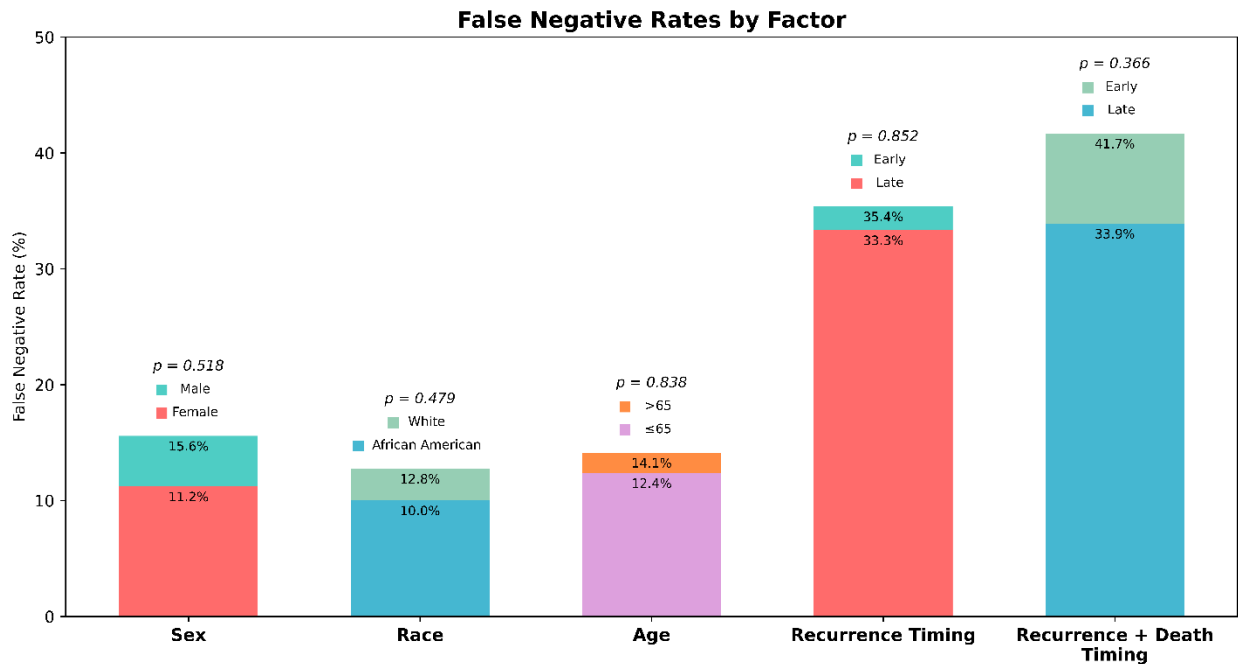


**Figure 6:** False negative rate analysis across demographic subgroups including age groups, showing higher rates in males (15.6%) and patients over 65 years (14.1%) and clinical timeline subgroups, with particularly high rates in the "Early Recurrence + Early Death" group (41.7%), highlighting the challenge of identifying aggressive disease patterns.

Across all tests, no statistically significant differences were found, indicating that the model is not demonstrably biased across sex, race, or age groups, and does not systematically fail for specific recurrence or mortality patterns. However, we note that the elevated false negative rate

in patients with early recurrence and early death may warrant closer inspection in future studies. The results are summarized in Figure 6.

### 3.9 Subgroup Analysis of Model Performance

To assess the fairness and generalizability of CellEcoNet across different demographic and clinical subpopulations, we conducted a subgroup analysis without stratifying patients based on any of these variables during train-test splits. Specifically, we evaluated model performance across groups defined by age, sex, race, tumor stage, and tumor grade. The results (summarized in Table 5) demonstrate that the model performs consistently across most subgroups, suggesting that it is not biased toward any particular demographic or clinical category. For instance, the model achieves comparable AUCs for males (0.75) and females (0.71), and performs similarly for African American (AUC = 0.77) and White patients (AUC = 0.76). Among age-based groups, older patients (Age  $\geq$  65) showed slightly better performance (AUC = 0.81) than younger ones (Age < 65, AUC = 0.70). Additionally, tumor grade and stage groups largely followed expected trends in performance, with New Grade G1 achieving the highest AUC (0.87) and Stage III suffering from low AUC (0.53) and accuracy (0.53).

Importantly, these analyses highlight that certain subgroups, such as Stage III patients, suffer from poor performance primarily due to limited representation in the dataset (N = 15). In some cross-validation folds, there were no Stage III patients in the training set, which likely contributed to the model's inability to generalize to this subgroup. These findings suggest that more balanced representation across all subgroups during model training could further improve performance and reduce variability. Incorporating stratified sampling or data augmentation strategies to ensure all subgroups are adequately represented in training could be a promising direction for future work.

**Table 5:** Subgroup-wise performance metrics of the model across demographic and clinical variables. *N* denotes the number of patients in each subgroup. The results are reported by combining the test splits from all cross-validation folds, ensuring complete coverage of the dataset. "Old Grade" refers to the traditional predominant pattern-based grading system in WHO 4<sup>th</sup> Ed. (2015), whereas "New Grade" corresponds to the IASLC grading system in WHO 5<sup>th</sup> Ed. (2021). Metrics reported include AUC, accuracy, sensitivity, and specificity, computed separately for each subgroup to evaluate model fairness and robustness.

Subgroup	N	Accuracy	Sensitivity	Specificity	AUC
White	149	71.14	66.67	73.91	75.93
African American	20	65.00	75.00	58.33	77.08
Age < 65	100	66.00	64.71	66.67	69.56
Age $\geq$ 65	89	74.16	65.79	80.39	80.70
Female	107	69.16	61.29	72.37	71.43
Male	77	70.13	69.23	71.05	75.44
New Grade G1	24	87.50	100.00	86.96	86.96
New Grade G2	53	73.58	70.00	74.42	73.26
New Grade G3	112	64.29	63.93	64.71	69.98
Old Grade G1	57	75.44	60.00	78.72	69.36
Old Grade G2	102	70.59	70.83	70.37	77.78

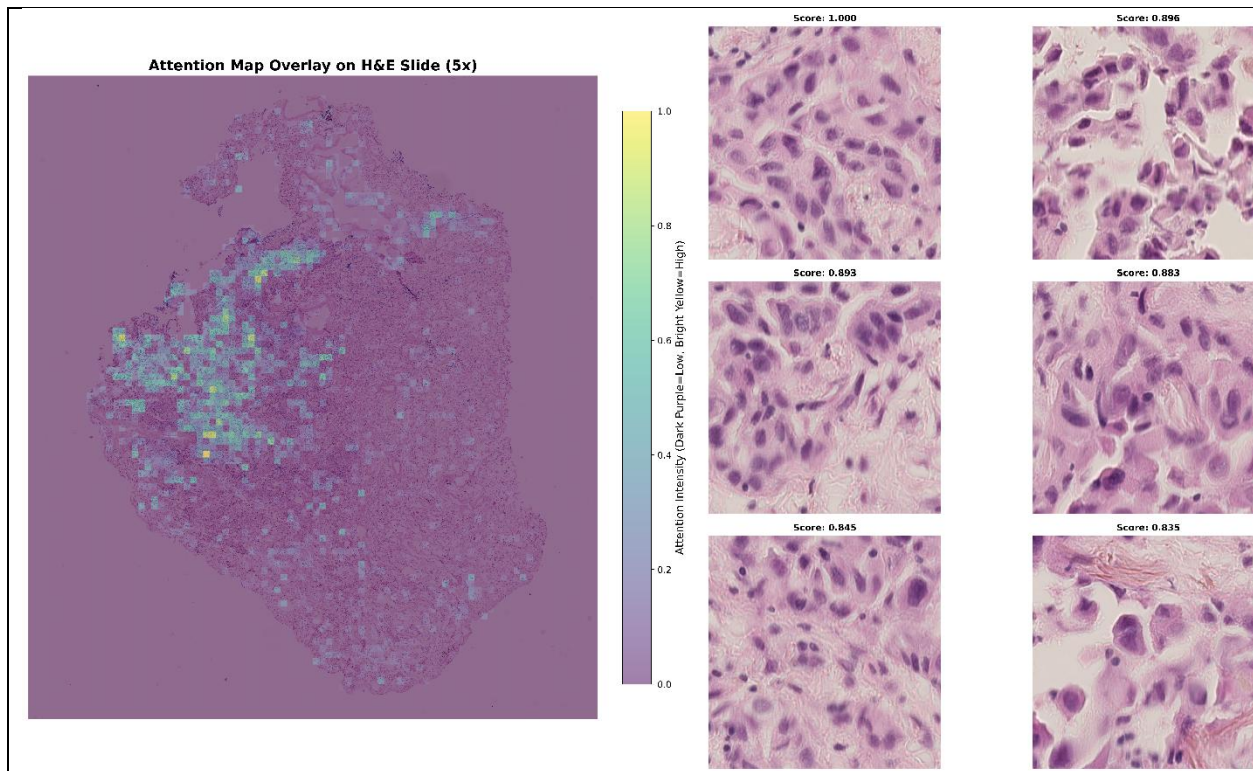
Old Grade G3	28	60.71	53.85	66.67	62.05
Stage I	130	73.85	64.86	77.42	75.12
Stage II	41	65.85	69.57	61.11	69.57
Stage III	15	53.33	58.33	33.33	52.78

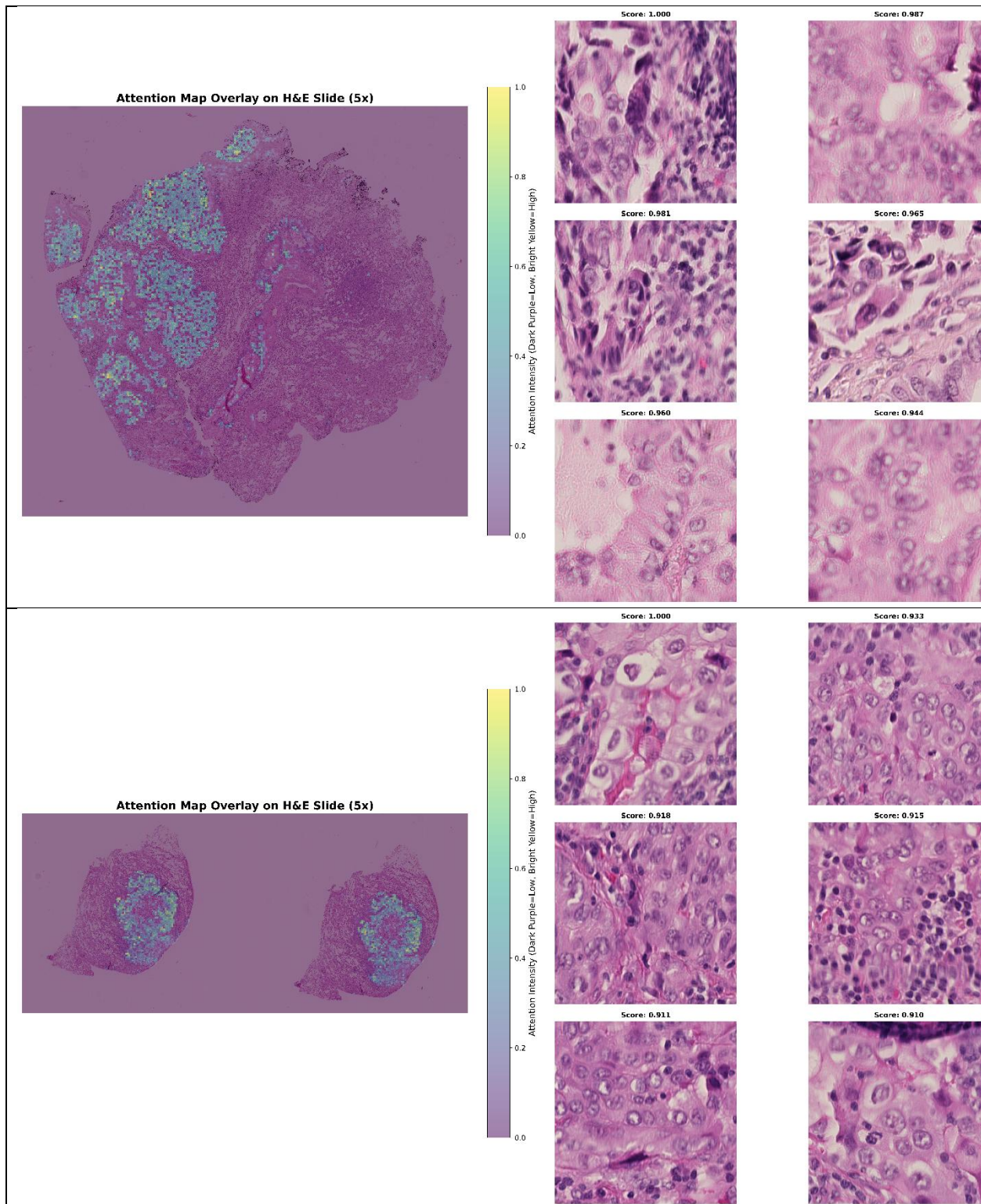
## 4 Interpretability of CellEcoNet via Attention Maps

To better understand the decision-making process of CellEcoNet, we generated attention maps highlighting the most influential regions in the model's recurrence predictions. These visualizations serve to provide interpretability and support clinical validation by illustrating which tissue compartments the model focuses on when classifying patients as likely to recur or not.

### 4.1 Attention Patterns in Recurred Patients

In patients correctly predicted to recur, the model often focused on histologic regions associated with high-risk pathological features. These included areas with solid or micropapillary growth patterns, poorly differentiated tumor morphology, nuclear atypia, and infiltrative tumor edges. Such features are known to correlate with poor prognosis and are frequently flagged by pathologists. Notably, the attention maps also captured peritumoral stroma and necrosis in several cases, suggesting that the model may be integrating contextual information from the tumor microenvironment. Figure 7 illustrates representative attention maps from three recurred patients. In each case, the heatmaps highlight the most influential regions contributing to the recurrence prediction, with warmer colors indicating higher attention scores.

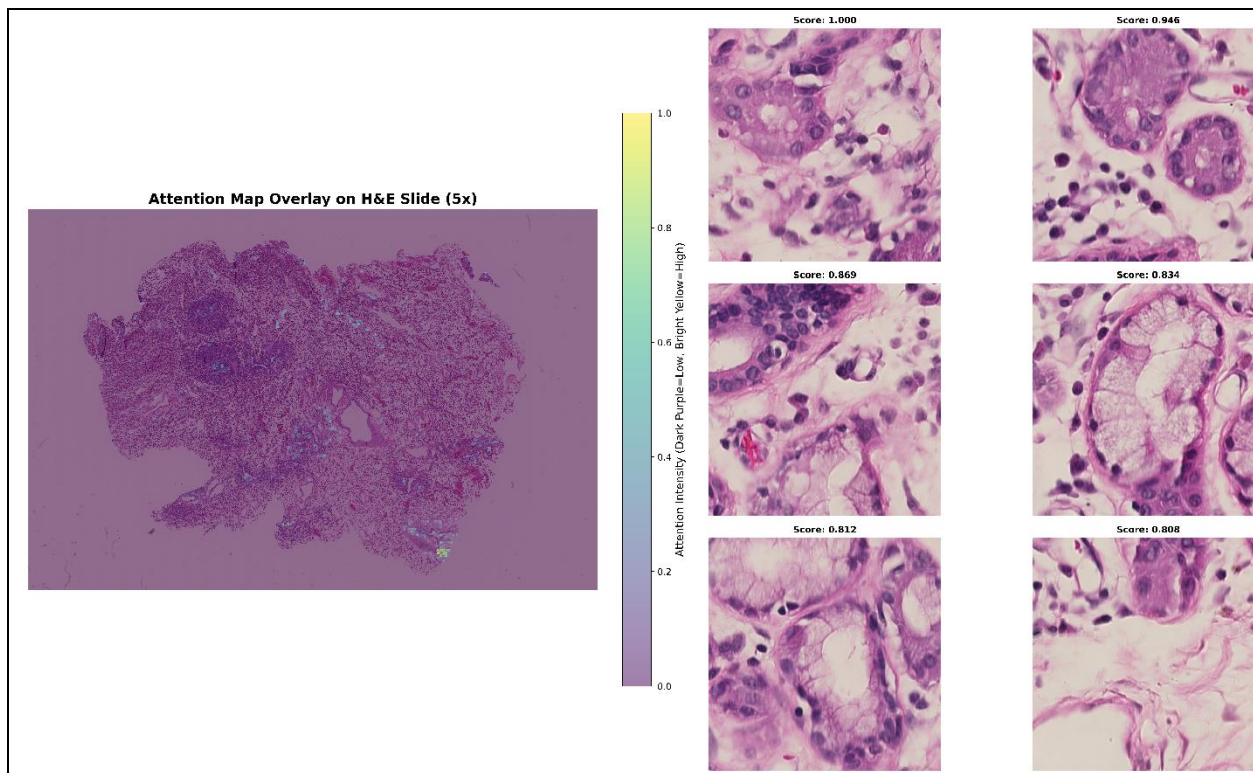




**Figure 7:** Attention maps for three correctly predicted recurred patients. In each row, a representative WSI's attention map is shown alongside its topmost highly attended patches. These patterns are all consistent with known poor prognostic indicators.

## 4.2 Attention Patterns in Non-Recurred Patients

In contrast, for patients correctly predicted not to recur, the model often attended to non-neoplastic elements, including lymphoid aggregates, fibrosis, plasma cells, histiocytes, and low-grade tumor regions. This suggests the model is able to identify features that reflect a favorable tumor microenvironment or less aggressive tumor biology, aligning with clinical expectations. These findings further underscore the model's ability to detect subtle but biologically meaningful histologic cues. Figure 8 shows attention maps for three correctly predicted non-recurred patients, where attention is predominantly placed on benign, immune-rich, or low-grade regions.



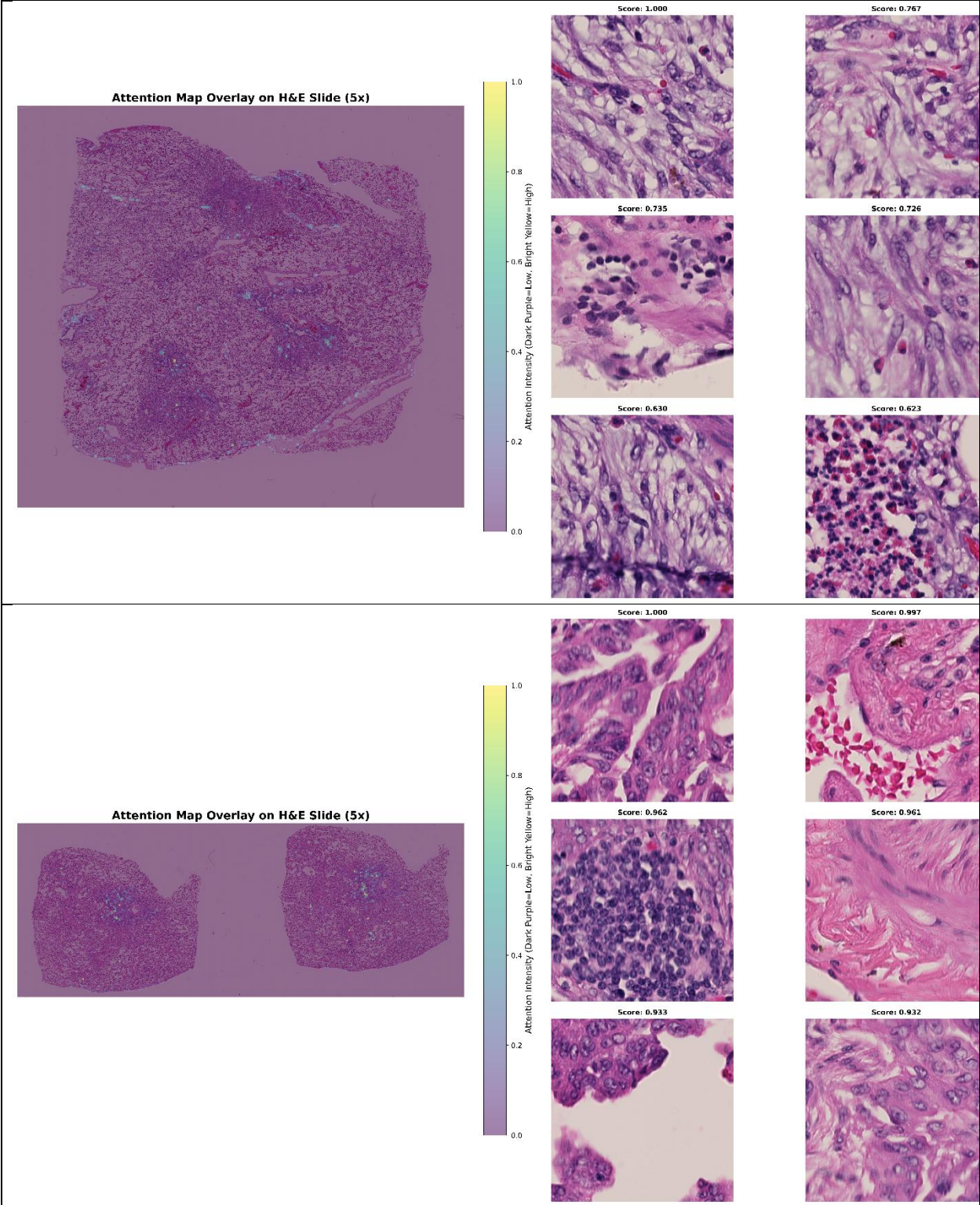
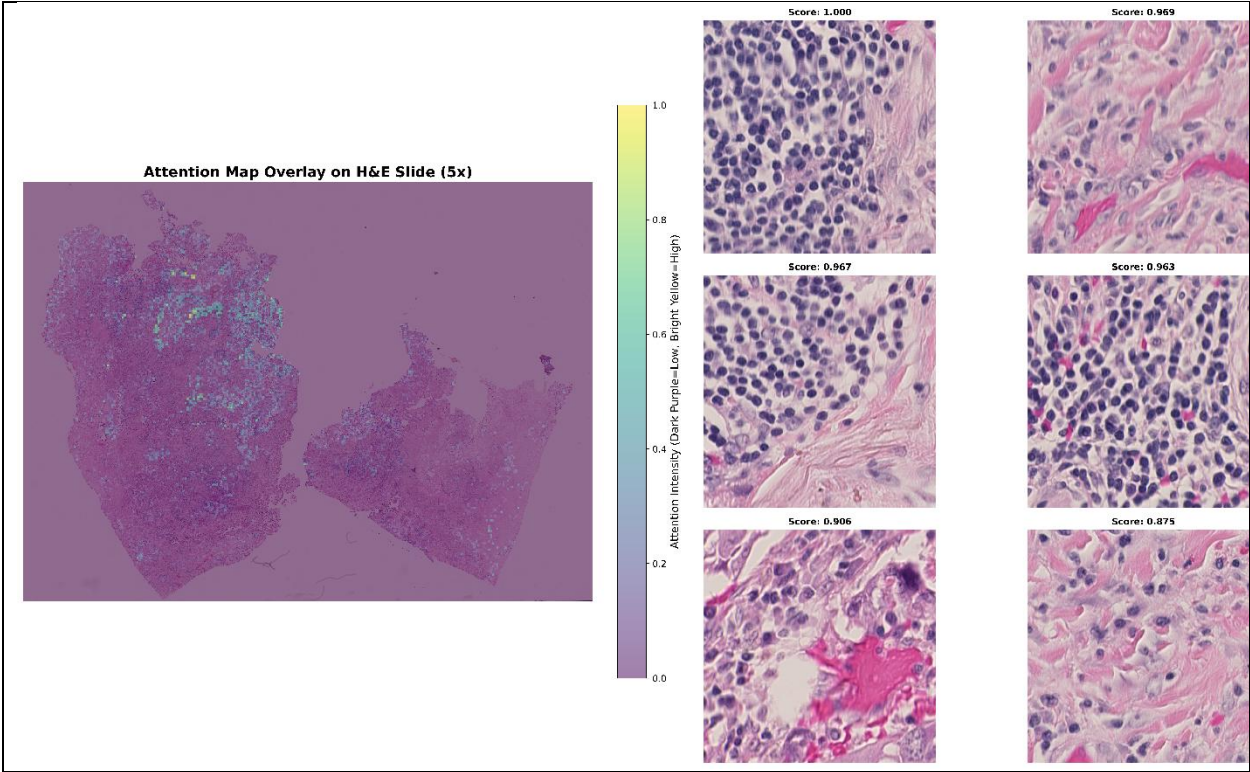


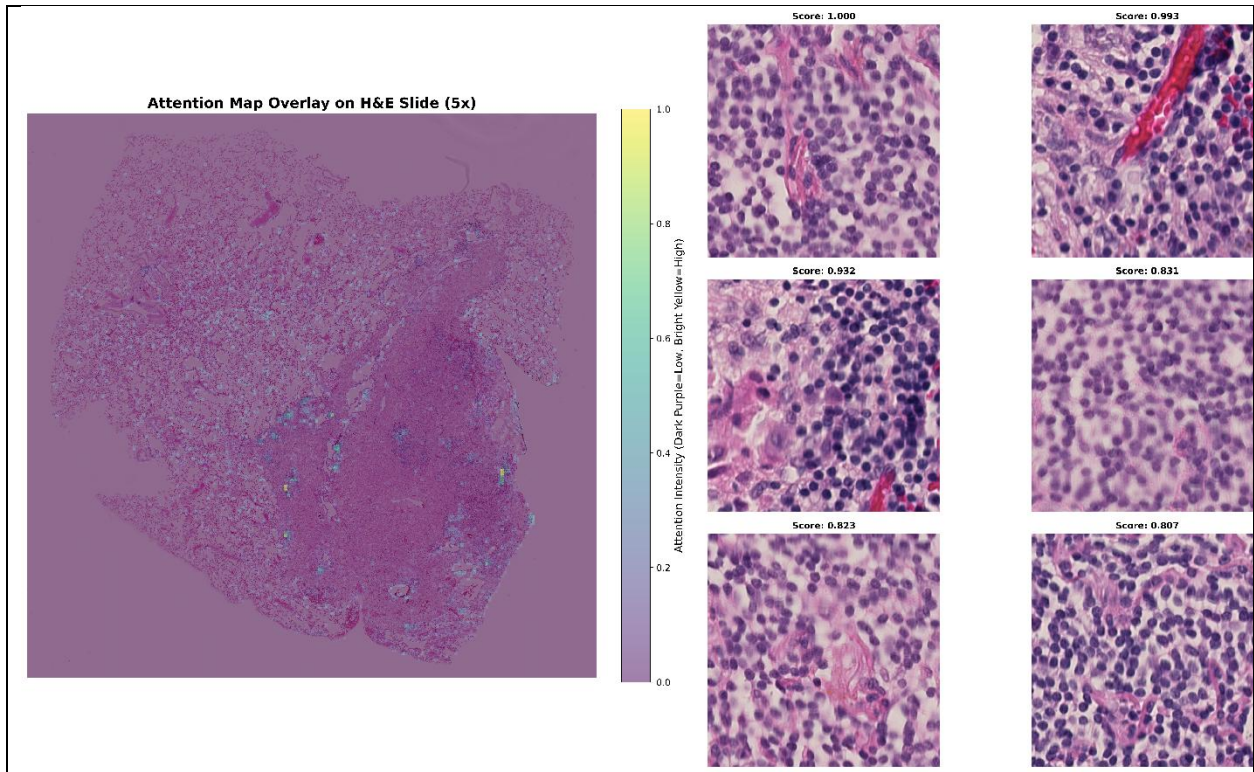
**Figure 8:** Attention maps for three correctly predicted non-recurred patients. These patterns suggest the model integrates microenvironmental cues in its risk assessment.

### 4.3 Less Interpretable Attention Patterns

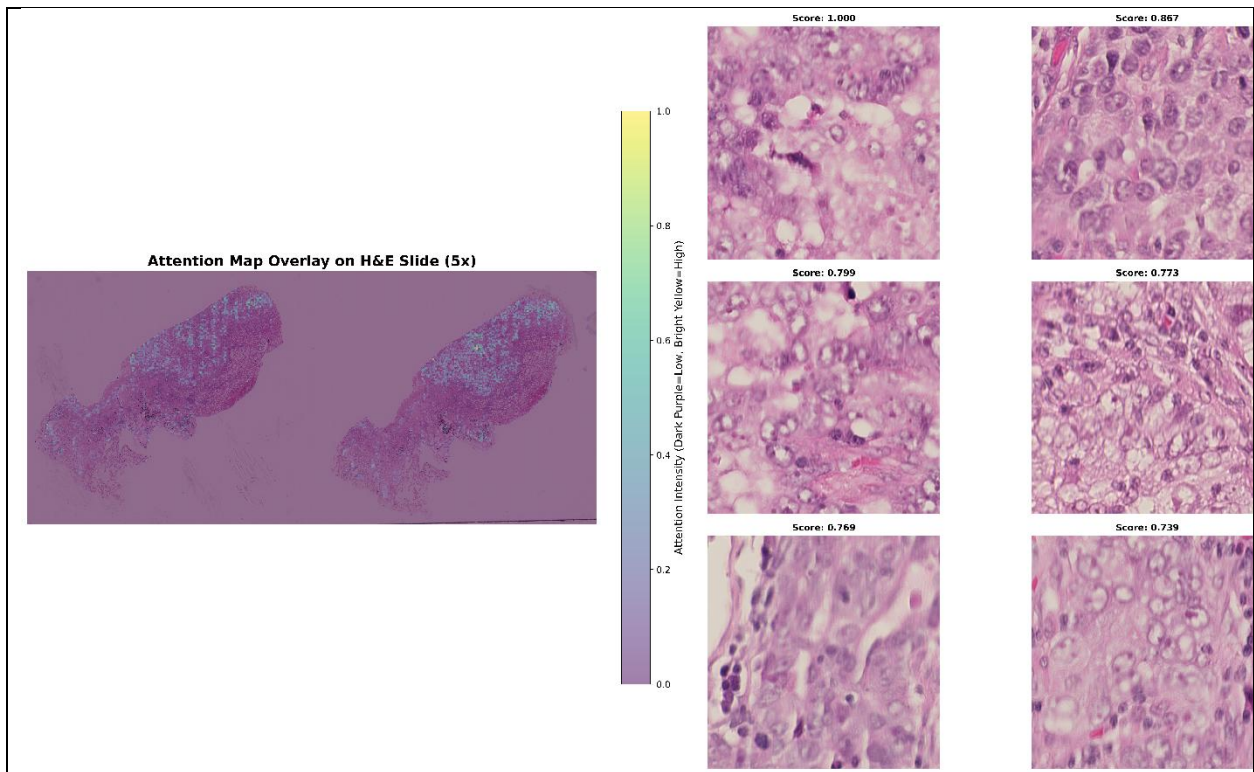
While most attention maps aligned with known pathologic features, we observed a subset of cases where the model’s focus was less clinically intuitive. In some recurred patients, the model attended primarily to non-neoplastic regions, such as lymphocytes or stromal tissue, despite the presence of aggressive tumor elsewhere. Conversely, in some non-recurred patients, the attention maps highlighted aggressive-appearing tumor regions without immune infiltrate.

These outliers may reflect the model’s recognition of sub-visual features—patterns not readily interpretable by human experts—or may be due to dataset-level statistical biases not immediately apparent. Further research is required to investigate whether these "unusual" attention patterns reflect novel prognostic cues or limitations of our model. Figure 9 presents two examples from recurred patients where attention maps focus on non-neoplastic areas, while Figure 10 shows two non-recurred cases where the model attended to regions of aggressive tumor morphology.





**Figure 9:** Attention maps from recurred patients with less interpretable focus. These cases raise questions about potential sub-visual features captured by the model.



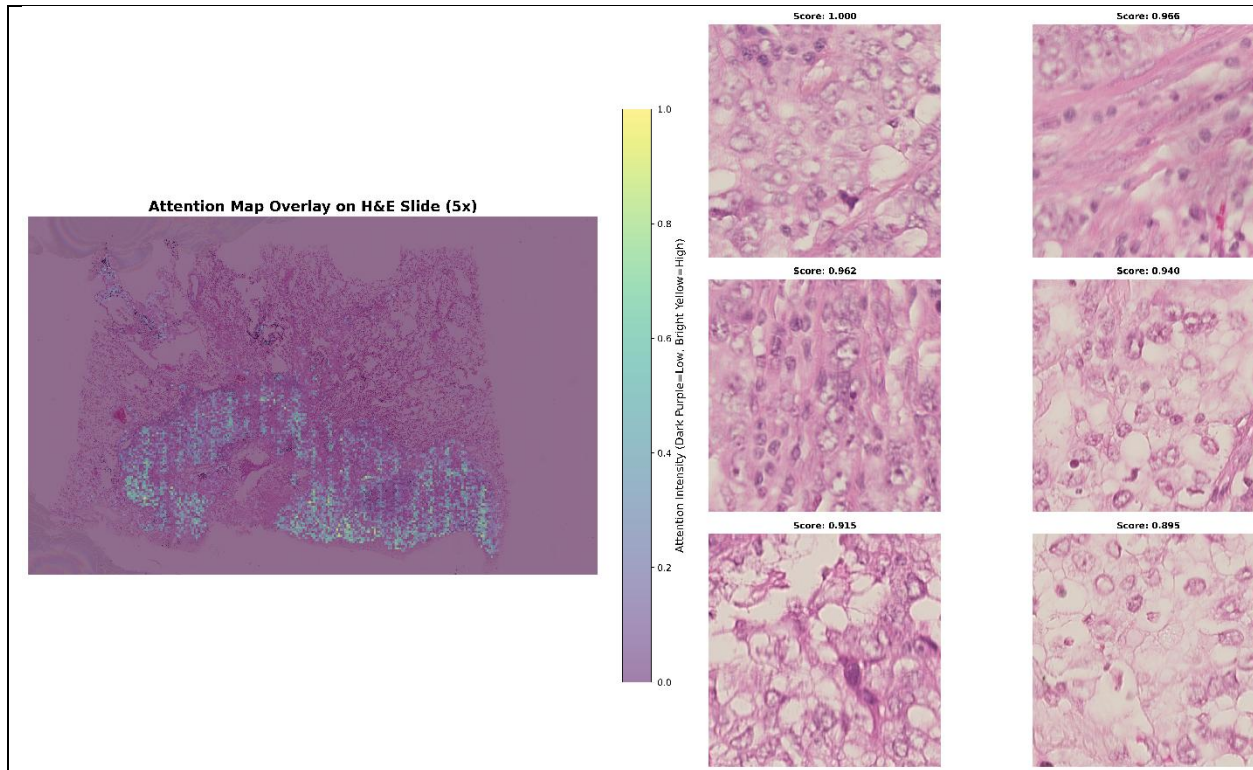


**Figure 10:** Attention maps from non-recurred patients with unexpected attention to aggressive areas. These cases might reflect the model's sensitivity to aggressive morphology even when it is not clinically predictive of recurrence in that patient.

## 5 Discussion

Traditional histopathology models treat WSIs as a collection of patches, ignoring the basic biological reality that cancer is a cellular disease [41]. Yet tumors comprise heterogeneous cellular populations with subtle morphological and molecular differences. Prior studies demonstrate that nuclear shape, texture, and size, features often too subtle for the human eye, can carry strong prognostic value [42, 43]. Moreover, TME includes dynamic populations of stromal, immune, and epithelial cells that modulate disease progression and therapeutic response. Together, these findings suggest that cell-level heterogeneity and interactions must be explicitly modeled to predict cancer outcomes accurately.

CellEcoNet operationalizes this concept by treating individual cells as the basic "tokens" of a pathological language. Just as language models derive meaning from the sequential arrangement of words, CellEcoNet learns the spatial and morphological relationships among cells as a biological "sentence" that encodes the state of the tumor ecosystem. The framework captures not only the type and state of each cell, but also the context in which it exists, a factor often overlooked by patch-based models.

To illustrate this, we extracted cell-level embeddings using the CellViT++ [26, 27] model for five major cell categories and compared the embeddings of the same cell type between patients with and without tumor recurrence. Figure 11 shows 3D t-SNE projections of benign epithelial cell

embeddings from randomly selected recurrence-positive (red) and recurrence-negative (blue) ILA patients. Although human pathologists would classify all these cells simply as benign epithelium, CellViT++ embeddings reveal clear separation—the red cluster occupies a distinct region of the embedding space compared to the blue cluster. Similar variation patterns were observed for other cell types.

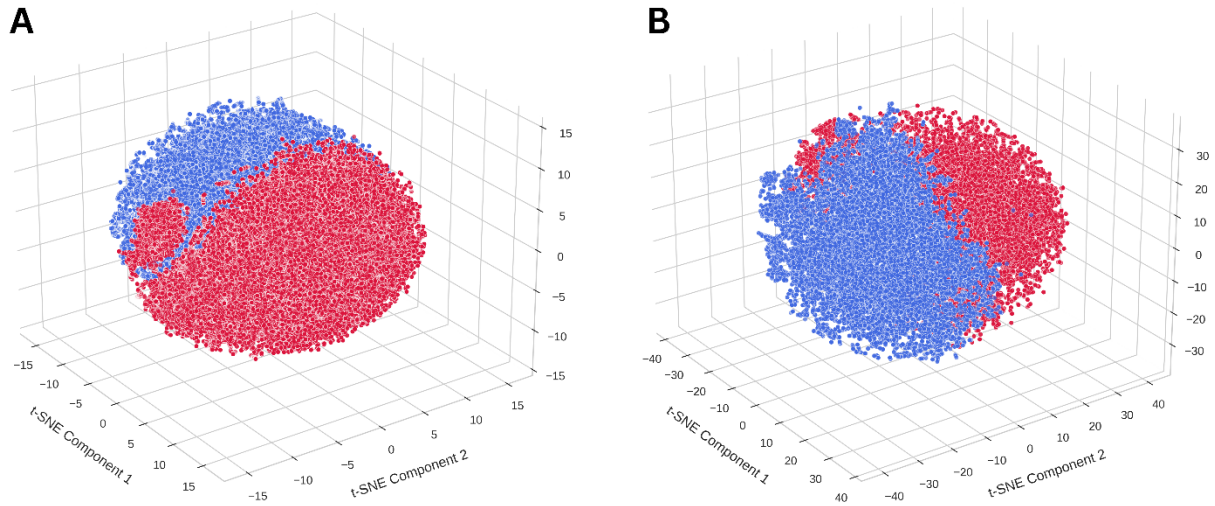


**Figure 11:** Each plot is a 3D t-SNE visualization of CellViT++ embeddings for benign epithelial cells from two randomly selected ILA patients (blue: no recurrence, red: recurrence). (A) shows two randomly selected patients based on a fixed seed, (B) shows two other patients selected on a different seed. Even within this single cell type, we observe distinct clusters corresponding to patient class, indicating intra- and inter-patient heterogeneity that correlates with outcome.

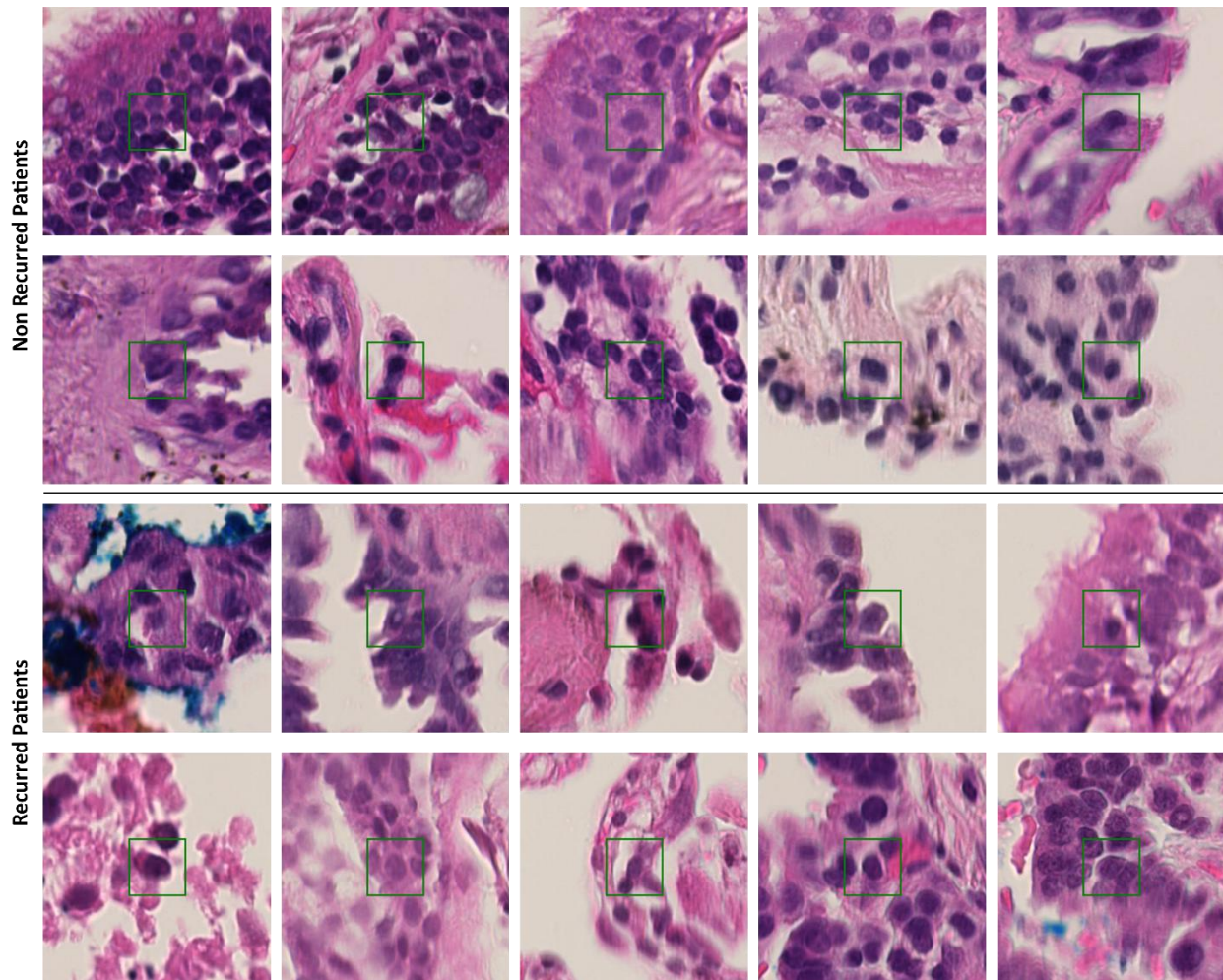


**Figure 12:** This figure displays sample cells from recurrent and non-recurrent patients, encoded differently by CellViT++, leading to their distinct spatial separation in the 3D t-SNE embedding space (Figure 11).

This variability reveals a rich landscape of sub-visual cellular heterogeneity. These subtle differences likely reflect underlying molecular and functional states that, while not visibly apparent, influence cancer progression and recurrence risk. This aligns with the emerging understanding that cancer is not just a disease of aberrant morphology but of complex cellular states and interactions that may lack obvious visual features. Such variability suggests that conventional visual-based cell typing may be insufficient for capturing the full spectrum of prognostically relevant cellular states. By operating in high-dimensional feature spaces, our approach detects and leverages these subtle differences, which would otherwise escape human perception.

The substantial performance improvements of CellEcoNet over state-of-the-art methods underscore the fundamental advantage of our multi-scale, cell-aware approach over conventional patch-based methods that lack explicit cellular modeling. Traditional MIL approaches treat tissue patches as atomic units, essentially averaging cellular information within each patch and losing the fine-grained morphological and spatial details that our results demonstrate are critical for

accurate recurrence prediction. By contrast, CellEcoNet's explicit cellular modeling preserves the individual identity and spatial relationships of cells, enabling the capture of subtle cellular phenotypes, local cellular neighborhoods, and cell-cell interaction patterns that are diluted or entirely lost in patch-level aggregation approaches.

While individual cells encode important morphological information, their spatial relationships constitute the structural framework that determines pathological significance. Cells in tissue organize into structured neighborhoods that reflect the underlying biology of tumor progression, immune response, and stromal remodeling. Through our patch-cell fusion mechanism, CellEcoNet models not only which cells are present, but also how they are arranged, enabling the framework to capture biologically important phenomena such as tumor-immune interactions, desmoplastic responses, and precursor epithelial lesions. The proximity of inflammatory cells to tumor cells may indicate immune surveillance or suppression, depending on the context. Similarly, the patterning of fibroblasts or dead cells can reflect active remodeling or necrosis, key indicators of aggressiveness.

This modeling approach is quantitatively validated in our results: the patch-cell fusion model outperformed cell-only and patch-only baselines by large margins (AUC: 74.28% vs. 64.28% and 67.47%, respectively), demonstrating that recurrence risk is determined not solely by cell presence, but by how these cells interact and are spatially arranged.

The ability of CellEcoNet to stratify patients into distinct risk groups has important implications for precision oncology. The substantial HR achieved by our Combined model (HR: 9.54, 95% CI: 4.34-20.98) indicates that patients classified as high-risk have nearly a ten-fold higher likelihood of recurrence compared to those classified as low-risk. This clear risk stratification could guide clinical decision-making regarding adjuvant therapy, surveillance intensity, and follow-up protocols for early-stage ILA patients, where treatment decisions remain challenging.

The superior performance of benign epithelial cell modeling (AUC: 74.98%) provides compelling evidence that benign epithelial cell morphology and spatial organization contain critical prognostic information previously underappreciated in lung adenocarcinoma recurrence prediction. This challenges the conventional focus on neoplastic cells alone, suggesting that apparently "normal" epithelial cells within the tumor microenvironment may reflect early molecular changes, field effects, or adaptive responses that precede malignant transformation. The success of individual cell-type models demonstrates that different cellular populations encode complementary prognostic information, with each cell type contributing unique insights into TME dynamics that influence disease progression.

Furthermore, cell-type specific insights could inform targeted therapy development. The strong prognostic signal from epithelial cells suggests that therapies targeting epithelial-specific vulnerabilities might be particularly effective in high-risk patients, while the prognostic relevance of inflammatory cells highlights the potential of immunotherapeutic approaches tailored to specific immune contextures.

## 5.1 Limitations and Future Directions

Despite the promising results, our study has several limitations. First, our dataset, while substantial, is from a single institution, which may limit the generalizability of our findings. External validation on multi-institutional cohorts is needed to confirm the robustness of our approach across different patient populations and imaging protocols.

Second, the temporal boundary challenge, the "recurrence cliff" phenomenon where patients who recur just before or after the 60-month cutoff receive different labels despite minimal biological difference, remains a limitation of binary classification approaches. Future work could explore continuous time-to-event modeling to address this issue more effectively.

Third, while our cell-type classification is more granular than most existing approaches, it still represents a simplification of the complex cellular composition of the TME. More detailed cell typing, potentially incorporating molecular markers through multiplex immunofluorescence or spatial transcriptomics, could further enhance the biological resolution and prognostic power of our approach.

Finally, the interpretability of DL models remains a challenge. Although our cell-type specific approach provides some level of biological interpretability, further work is needed to identify the specific morphological and spatial features that drive prognostic predictions.

Future directions include integrating molecular data (genomics, transcriptomics, proteomics) with our imaging-based approach to create multimodal prognostic models that capture both morphological and molecular determinants of recurrence risk. Additionally, extending our framework to other cancer types and clinical endpoints (overall survival, response to specific therapies) could broaden its clinical utility.

## 6 Conclusions

CellEcoNet represents a significant advance in computational pathology by bridging the cellular information gap in TME analysis. While cells may appear visually similar under the microscope, our computational approach reveals subtle yet prognostically critical differences in cellular composition, morphology, and most importantly, the spatial organization. By explicitly modeling cellular adjacency, proximity, and collective arrangement, CellEcoNet captures multicellular interactions that conventional patch-based methods miss, providing superior prognostic performance.

Our results demonstrate that cell-level analysis, particularly when integrated with tissue-level context through our patch-cell fusion mechanism, uncovers biological determinants of recurrence risk in ILA. Notably, cell-type-specific models reveal distinct and complementary insights like, benign epithelial cell characteristics exhibit strong predictive value, while the spatial interplay of diverse cell populations further refines risk stratification. The integration of these multicellular features through ensemble learning achieves substantially better performance than single cell-

type models, reflecting the complex biology of cancer progression. Clinically, this approach shows remarkable potential, with our ensemble model achieving a striking HR of 9.54, underscoring its utility in guiding treatment decisions.

Beyond improving recurrence prediction, CellEcoNet advances cancer biology by elucidating how cellular and spatial dynamics drive disease progression. These insights challenge traditional histopathological evaluation, demonstrating that computational pathology can uncover prognostic signals invisible to the human eye. By combining cellular resolution with tissue-scale context, our framework not only enhances prognostic accuracy but also opens new avenues for personalized therapeutic strategies, ultimately contributing to more effective cancer care.

Conceptually, CellEcoNet introduces a new framework for interpreting histopathology: one where cells are treated as the fundamental units of a biological language, and their spatial arrangement encodes meaning, function, and prognosis. By decoding this language with deep learning, we not only improve prediction but redefine how we understand tissue architecture, transforming pathology into a language that AI can read and clinicians can act upon.

## **Author contributions**

A. R. A. performed data preprocessing, designed and conducted experiments, validation, and manuscript writing. U. S. and Z. S. provided feedback on the study design and validation and also edited the manuscript. W. L, F. X., and J. R. performed data collection, provided clinical assessment, and contributed to the manuscript editing. W. C. and M.K.K.N. conceptualized and designed the study, provided study validation, supervised the research, and contributed to the manuscript writing and editing.

## **Acknowledgments**

The project described was supported in part by R01 CA276301 (PIs: Niazi and Chen) from the National Cancer Institute, R01 DC020715 (PIs: Moberly and Gurcan) from the National Institute on Deafness and Other Communication Disorders, and R01 HL177046-01 (PIs: Hachem, Gurcan, and Michelson) from the National Heart, Lung, and Blood Institute. The project was also supported partly by Pelotonia under IRP CC13702 (PIs: Niazi, Vilgelm, and Roy), The Ohio State University Department of Pathology and Comprehensive Cancer Center. The content is solely the responsibility of the authors and does not necessarily represent the official views of the National Cancer Institute or National Institutes of Health or The Ohio State University.

## **Competing Interests**

All authors declare no financial or non-financial competing interests.

## **Data Availability**

The data that support the findings of this study are available from Wake Forest Baptist Comprehensive Cancer Center, but restrictions apply to the availability of these data, which were

used under license for the current study, and so are not publicly available. Data are, however, available from the authors upon reasonable request and with permission of Wake Forest Baptist Comprehensive Cancer Center.

## Code Availability

The underlying code for this study is available in AI4Path CellEcoNet repository and can be accessed via this link <https://github.com/AI4Path-Lab/CellEcoNet>

- [1] R. L. Siegel, T. B. Kratzer, A. N. Giaquinto, H. Sung, and A. Jemal, "Cancer statistics, 2025," *Ca*, vol. 75, no. 1, p. 10, 2025.
- [2] F. Bray *et al.*, "Global cancer statistics 2022: GLOBOCAN estimates of incidence and mortality worldwide for 36 cancers in 185 countries," *CA: a cancer journal for clinicians*, vol. 74, no. 3, pp. 229-263, 2024.
- [3] P. Goldstraw *et al.*, "The IASLC lung cancer staging project: proposals for revision of the TNM stage groupings in the forthcoming (eighth) edition of the TNM classification for lung cancer," *Journal of Thoracic Oncology*, vol. 11, no. 1, pp. 39-51, 2016.
- [4] M. D. Hellmann *et al.*, "Circulating tumor DNA analysis to assess risk of progression after long-term response to PD-(L) 1 blockade in NSCLC," *Clinical Cancer Research*, vol. 26, no. 12, pp. 2849-2858, 2020.
- [5] J.-P. Pignon *et al.*, "Lung adjuvant cisplatin evaluation: a pooled analysis by the LACE Collaborative Group," *Journal of clinical oncology*, vol. 26, no. 21, pp. 3552-3559, 2008.
- [6] R. Arriagada *et al.*, "Long-term results of the international adjuvant lung cancer trial evaluating adjuvant Cisplatin-based chemotherapy in resected lung cancer," *Journal of clinical oncology*, vol. 28, no. 1, pp. 35-42, 2010.
- [7] D. Wankhede, "Evaluation of Eighth AJCC TNM Stage for Lung Cancer NSCLC: A Meta-analysis," (in eng), *Ann Surg Oncol*, vol. 28, no. 1, pp. 142-147, Jan 2021, doi: 10.1245/s10434-020-09151-9.
- [8] K. Chen, H. Chen, F. Yang, X. Sui, X. Li, and J. Wang, "Validation of the Eighth Edition of the TNM Staging System for Lung Cancer in 2043 Surgically Treated Patients With Non-small-cell Lung Cancer," (in eng), *Clin Lung Cancer*, vol. 18, no. 6, pp. e457-e466, Nov 2017, doi: 10.1016/j.clcc.2017.04.001.
- [9] J. K. Yun *et al.*, "Validation of the 8th edition of the TNM staging system in 3,950 patients with surgically resected non-small cell lung cancer," (in eng), *J Thorac Dis*, vol. 11, no. 7, pp. 2955-2964, Jul 2019, doi: 10.21037/jtd.2019.07.43.
- [10] P. Huang *et al.*, "MA03.04 An Integrated Deep Learning Method to Predict Lung Cancer Recurrence Risk for Resected Stage IA NSCLC," *Journal of Thoracic Oncology*, vol. 17, no. 9, pp. S50-S51, 2022, doi: 10.1016/j.jtho.2022.07.089.
- [11] Y. Wang *et al.*, "IASLC grading system predicts distant metastases for resected lung adenocarcinoma," *Journal of Clinical Pathology*, pp. jcp-2024-209649, 2024, doi: 10.1136/jcp-2024-209649.

- [12] A. L. Moreira *et al.*, "A Grading System for Invasive Pulmonary Adenocarcinoma: A Proposal From the International Association for the Study of Lung Cancer Pathology Committee," *J Thorac Oncol*, vol. 15, no. 10, pp. 1599-1610, Oct 2020, doi: 10.1016/j.jtho.2020.06.001.
- [13] E. Haoran *et al.*, "The IASLC grading system for invasive pulmonary adenocarcinoma: a potential prognosticator for patients receiving neoadjuvant therapy," *Therapeutic Advances in Medical Oncology*, vol. 15, 2023.
- [14] M. K. K. Niazi, A. V. Parwani, and M. N. Gurcan, "Digital pathology and artificial intelligence," *The lancet oncology*, vol. 20, no. 5, pp. e253-e261, 2019.
- [15] A. Echle, N. T. Rindtorff, T. J. Brinker, T. Luedde, A. T. Pearson, and J. N. Kather, "Deep learning in cancer pathology: a new generation of clinical biomarkers," *British journal of cancer*, vol. 124, no. 4, pp. 686-696, 2021.
- [16] K. Bera, K. A. Schalper, D. L. Rimm, V. Velcheti, and A. Madabhushi, "Artificial intelligence in digital pathology—new tools for diagnosis and precision oncology," *Nature reviews Clinical oncology*, vol. 16, no. 11, pp. 703-715, 2019.
- [17] S. Alfasly, G. Alabtah, S. Hemati, K. R. Kalari, and H. Tizhoosh, "Zero-Shot Whole Slide Image Retrieval in Histopathology Using Embeddings of Foundation Models," *arXiv preprint arXiv:2409.04631*, 2024.
- [18] C. L. Srinidhi, O. Ciga, and A. L. Martel, "Deep neural network models for computational histopathology: A survey," *Medical image analysis*, vol. 67, p. 101813, 2021.
- [19] O. Maron and T. Lozano-Pérez, "A framework for multiple-instance learning," *Advances in neural information processing systems*, pp. 570-576, 1998.
- [20] M. Ilse, J. Tomczak, and M. Welling, "Attention-based deep multiple instance learning," in *International conference on machine learning*, 2018: PMLR, pp. 2127-2136.
- [21] M. Y. Lu, D. F. Williamson, T. Y. Chen, R. J. Chen, M. Barbieri, and F. Mahmood, "Data-efficient and weakly supervised computational pathology on whole-slide images," *Nature biomedical engineering*, vol. 5, no. 6, pp. 555-570, 2021.
- [22] Z. Shao, H. Bian, Y. Chen, Y. Wang, J. Zhang, and X. Ji, "Transmil: Transformer based correlated multiple instance learning for whole slide image classification," *Advances in Neural Information Processing Systems*, vol. 34, pp. 2136-2147, 2021.
- [23] Z. Su, M. Rezapour, U. Sajjad, S. Niu, M. N. Gurcan, and M. K. K. Niazi, "Cross-attention-based saliency inference for predicting cancer metastasis on whole slide images," *arXiv preprint arXiv:2309.09412*, 2023.
- [24] J. Mao *et al.*, "CAMIL: channel attention-based multiple instance learning for whole slide image classification," *Bioinformatics*, vol. 41, no. 2, 2025, doi: 10.1093/bioinformatics/btaf024.
- [25] S. Graham *et al.*, "Hover-net: Simultaneous segmentation and classification of nuclei in multi-tissue histology images," *Medical image analysis*, vol. 58, p. 101563, 2019.
- [26] F. Hörst *et al.*, "Cellvit: Vision transformers for precise cell segmentation and classification," *Medical Image Analysis*, vol. 94, p. 103143, 2024.

- [27] F. Hörst, M. Rempe, H. Becker, L. Heine, J. Keyl, and J. Kleesiek, "CellViT++: Energy-Efficient and Adaptive Cell Segmentation and Classification Using Foundation Models," *arXiv preprint arXiv:2501.05269*, 2025.
- [28] H. Uramoto and F. Tanaka, "Recurrence after surgery in patients with NSCLC," *Translational lung cancer research*, vol. 3, no. 4, p. 242, 2014.
- [29] W. D. Travis *et al.*, "International association for the study of lung cancer/american thoracic society/european respiratory society international multidisciplinary classification of lung adenocarcinoma," *Journal of thoracic oncology*, vol. 6, no. 2, pp. 244-285, 2011.
- [30] A. Yoshizawa *et al.*, "Impact of proposed IASLC/ATS/ERS classification of lung adenocarcinoma: prognostic subgroups and implications for further revision of staging based on analysis of 514 stage I cases," *Mod Pathol*, vol. 24, no. 5, pp. 653-64, May 2011, doi: 10.1038/modpathol.2010.232.
- [31] K. Kadota *et al.*, "Tumor spread through air spaces is an important pattern of invasion and impacts the frequency and location of recurrences after limited resection for small stage I lung adenocarcinomas," *Journal of Thoracic Oncology*, vol. 10, no. 5, pp. 806-814, 2015.
- [32] E. Thunnissen *et al.*, "Reproducibility of histopathological subtypes and invasion in pulmonary adenocarcinoma. An international interobserver study," *Modern pathology*, vol. 25, no. 12, pp. 1574-1583, 2012.
- [33] J. Zhang *et al.*, "Intratumor heterogeneity in localized lung adenocarcinomas delineated by multiregion sequencing," *Science*, vol. 346, no. 6206, pp. 256-259, 2014.
- [34] P.-J. Kim *et al.*, "A new model using deep learning to predict recurrence after surgical resection of lung adenocarcinoma," *Scientific reports*, vol. 14, no. 1, p. 6366, 2024.
- [35] Z. Su *et al.*, "Deep Learning Model for Predicting Lung Adenocarcinoma Recurrence from Whole Slide Images," *Cancers*, vol. 16, no. 17, p. 3097, 2024.
- [36] R. J. Chen *et al.*, "Towards a general-purpose foundation model for computational pathology," *Nature Medicine*, vol. 30, no. 3, pp. 850-862, 2024.
- [37] A. Zhang, G. Jaume, A. Vaidya, T. Ding, and F. Mahmood, "Accelerating Data Processing and Benchmarking of AI Models for Pathology," *arXiv preprint arXiv:2502.06750*, 2025.
- [38] A. Vaidya *et al.*, "Molecular-driven Foundation Model for Oncologic Pathology," *arXiv preprint arXiv:2501.16652*, 2025.
- [39] A. Kirillov *et al.*, "Segment anything," in *Proceedings of the IEEE/CVF international conference on computer vision*, 2023, pp. 4015-4026.
- [40] F. Hörst, S. H. Schaheer, G. Baldini, F. H. Bahnsen, J. Egger, and J. Kleesiek, "Accelerating Artificial Intelligence-based Whole Slide Image Analysis with an Optimized Preprocessing Pipeline," in *BVM Workshop, 2024*: Springer, pp. 356-361.
- [41] D. Li *et al.*, "Multi-Modal Foundation Models for Computational Pathology: A Survey," *arXiv preprint arXiv:2503.09091*, 2025.
- [42] R. Sali, Y. Jiang, A. Attaranzadeh, B. Holmes, and R. Li, "Morphological diversity of cancer cells predicts prognosis across tumor types," *JNCI: Journal of the National Cancer Institute*, vol. 116, no. 4, pp. 555-564, 2024.

- [43] J. Couetil, Z. Liu, K. Huang, J. Zhang, and A. K. Alomari, "Predicting melanoma survival and metastasis with interpretable histopathological features and machine learning models," *Frontiers in Medicine*, vol. 9, p. 1029227, 2023.